



1 **The variation and visualisation of elastic anisotropy in rock forming minerals**

2 David Healy¹, Nicholas E. Timms² & Mark A. Pearce³

3 ¹: School of Geosciences, King's College, University of Aberdeen, Aberdeen AB24 3UE, United
4 Kingdom

5 ²: Space Science and Technology Centre, School of Earth and Planetary Sciences, Curtin
6 University, Perth, GPO Box U1987, WA 6845, Australia

7 ³: CSIRO Mineral Resources, Australian Resources Research Centre, 26 Dick Perry Avenue,
8 Kensington, WA 6151, Australia

9 *corresponding author: d.healy@abdn.ac.uk

10

11 **Abstract**

12 All minerals behave elastically, a rheological property that controls their ability to support stress,
13 strain and pressure, the nature of acoustic wave propagation and influences subsequent plastic (i.e.
14 permanent, non-reversible) deformation. All minerals are intrinsically anisotropic in their elastic
15 properties – that is, they have directional variations that are related to the configuration of the
16 crystal lattice. This means that the commonly used mechanical elastic properties that relate elastic
17 stress to elastic strain, including Young's modulus (E), Poisson's ratio (ν), shear modulus (G) and
18 linear compressibility (β), are dependent on crystallographic direction. In this paper, we explore the
19 ranges of anisotropy of E , ν , G and β in 86 rock-forming minerals, using previously published data,
20 and show that the range is much wider than commonly assumed. We also explore how these
21 variations (the directionality and the magnitude) are important for fundamental processes in the
22 solid earth, including deformation (mechanical) twinning, coherent phase transformations and
23 brittle failure. We present a new open source software package (AnisoVis, written in MATLAB),
24 which we use to calculate and visualise directional variations in elastic properties of rock-forming
25 minerals. Following previous work in the fields of chemistry and materials, we demonstrate that by
26 visualising the variations in elasticity, we discover previously unreported properties of rock forming
27 minerals. For example, we show previously unreported directions of negative Poisson's ratio and
28 negative linear compressibility and we show that the existence of these features is more widespread
29 (i.e. present in many more minerals) than previously thought. We illustrate the consequences of
30 intrinsic elastic anisotropy for the elastic normal and shear strains within α -quartz single crystal
31 under different applied stress fields; the role of elastic anisotropy on Dauphiné twinning and the α -
32 β phase transformations in quartz; and stress distributions around voids of different shapes in talc,
33 lizardite, albite, and sanidine. In addition to our specific examples, elastic anisotropy in rock-
34 forming minerals to the degree that we describe has significant consequences for seismic (acoustic)
35 anisotropy, the focal mechanisms of earthquakes in anisotropic source regions (e.g. subducting
36 slabs), for a range of brittle and ductile deformation mechanisms in minerals, and geobarometry
37 using mineral inclusions.

38

39



40 Introduction

41 The elastic deformation of rock-forming minerals plays an important role in many earth processes.
42 The increased availability of measured or calculated elastic properties of whole rocks and of
43 specific rock-forming minerals has led to advances in many fields of earth science, including
44 seismology, geodynamics, tectonics and metamorphism. Minerals have long been known to display
45 anisotropy – directional variations – in their elastic properties (Mandell, 1927; Birch & Dancroft,
46 1938; Hearmon, 1946), and that these variations show a close relationship to the symmetry of the
47 mineral crystallographic structure. Advances in laboratory methods of measurement (acoustic
48 velocities, Brillouin scattering, resonant ultrasound) and in theoretical techniques for *ab initio*
49 calculations has allowed scientists to quantify this anisotropy for a wide range of rock forming
50 minerals. For this paper we have collected 246 published datasets (measurements or *ab initio*
51 calculations) of anisotropic elastic properties covering 86 distinct minerals. Elastic anisotropy is
52 fully described by a fourth rank tensor (compliance or stiffness, see below), and published data are
53 commonly presented in a Voigt matrix format, listing up to 21 independent values (depending on
54 the crystal symmetry class), whereas elastically isotropic minerals require only 2 independent
55 values. A key aim of this paper is to use published data to visualise and explore elastic anisotropy
56 in rock forming minerals using familiar measures, such as Young's modulus and Poisson's ratio,
57 but presented in novel formats and thereby render the increasing volume of data more transparent to
58 analysis. As noted by previous authors (Karki & Chennamsetty, 2006; Lethbridge et al., 2010;
59 Marmier et al., 2010; Gaillac et al., 2016), graphical depictions of the directional variation of elastic
60 properties provide new opportunities to relate the quantitative data to the crystalline structure of the
61 mineral. This in turn allows us to relate the observed or predicted mechanical and chemical
62 behaviour of the mineral to specific crystallographic directions.

63 It has long been recognized that the velocity of seismic waves passing through rocks is a direct
64 function of the minerals' elastic properties and their density, expressed through the Christoffel
65 equation (Christoffel, 1877; Zhou & Greenhalgh, 2004). By considering rocks as polycrystalline
66 aggregates various workers have modelled seismic velocities, and their anisotropy, by combining
67 single mineral elasticity data with different averaging schemes due to Reuss, Voigt or Hill (e.g.
68 Mainprice, 1990; Lloyd & Kendall, 2005). This 'rock recipe' approach has improved our
69 understanding of the composition and structure of the lower crust and mantle and provided useful
70 constraints for alternative models for observed variations in seismic anisotropy beneath continents
71 and around arcs (e.g. Kern, 1982; Tatham et al., 2008; Healy et al., 2009).

72 Inclusions of one mineral or fluid within another host mineral have been used to estimate pressures
73 at the time of inclusion or entrapment (Rosenfeld & Chase, 1961; Rosenfeld, 1969; Chopin, 1984;
74 Gillet et al., 1984; van der Molen & van Roermund, 1986; Angel et al., 2014; Angel et al., 2015).
75 The analysis critically depends on the elastic properties of the host mineral and, in the case of solid
76 inclusions, of the inclusion itself, typically expressed as the bulk and shear moduli (e.g.
77 Mazzucchelli et al., 2018). The underlying theory is based on the classical analysis by Eshelby
78 (1957, 1959) who derived the equations for the deformation within an ellipsoidal inclusion and host
79 due to the imposition of a far-field load. Most of the work to date has simplified the analysis to
80 assume isotropy in both the inclusion and the host, although see Zhang (1998) for a rare exception.
81 Therefore, the full effects of host minerals and inclusion elastic anisotropy on inclusion-based
82 geobarometry have not yet been rigorously investigated. Furthermore, fluid inclusions can
83 decrepitate – i.e. fracture their host and dissipate their fluid – if their internal overpressure rises to a



84 critical value that exceeds the local strength of the enclosing grain. The basis for predicting this
85 behaviour is linear elastic fracture mechanics (LEFM), and the assumption of elastic isotropy is
86 nearly ubiquitous (e.g. Lacazette, 1990).

87 Permanent, non-reversible (i.e. plastic) deformation of minerals is invariably preceded by an elastic
88 response prior to some form of yield condition being reached. For example, the elastic properties of
89 minerals are important in the analysis of brittle cracking at the grain scale. As noted above for the
90 decrepitation of fluid inclusions, the dominant paradigm for this analysis is linear elastic fracture
91 mechanics (LEFM), and the assumption of elastic isotropy. This is important because faults and
92 fractures in rocks are composite structures, built by the interaction and coalescence of many smaller
93 cracks that nucleate at the scale of individual grains i.e. within elastically anisotropic crystals.
94 Jaeger & Cook (1969) used the equations published by Green & Taylor (1939) to consider the
95 stresses developed at the edges of circular holes in anisotropic rocks. In their analysis (repeated in
96 Pollard & Fletcher, 2005), they dismissed the significance of elastic anisotropy because the ratio of
97 maximum to minimum Young's modulus in rocks is 'rarely as high as 2'. Timms et al. (2010)
98 conducted novel indentation experiments in a single crystal of quartz and produced a type of cone
99 fracture with variations in opening angle and crack length that have a trigonal symmetry radiating
100 from the point of contact, and thus demonstrated the key role played by the elastic anisotropy in
101 controlling the fracture geometry. In the same study, these authors confirmed that elastic
102 anisotropy plays a significant role in controlling the focal mechanisms (moment tensors) of acoustic
103 emission events at the scale of a single crystal.

104 Poisson's ratio appears as a term in, for example, the equations describing fracture toughness and
105 indentation, and therefore the precise value of Poisson's ratio is important. Poisson's ratio for
106 isotropic materials is constrained to lie between 0.5 and -1, but there are no theoretical limits for
107 anisotropic materials (Ting & Chen, 2005). Materials with Poisson's ratio less than 0 are termed
108 'auxetic' (Lakes, 1987; Baughman et al., 1998a; Prawoto, 2012; Pasternak & Dyskin, 2012).
109 Fracture toughness and resistance to indentation increase as Poisson's ratio approaches the lower
110 (isotropic) limit of -1.0 (Yeganeh-Haeri et al., 1992). In rock forming minerals, negative Poisson's
111 ratios have already been documented for α -cristobalite (Yeganeh-Haeri et al., 1992), for quartz at
112 the α - β phase transition (Mainprice & Casey, 1990), for talc (Mainprice et al., 2008), and for calcite
113 and aragonite (Aouni & Wheeler, 2008). A key question therefore is to determine if there are other
114 rock forming minerals with the same properties, and for which specific crystallographic directions.
115 In a recent review of data on Poisson's ratio in engineering materials, Greaves et al. (2011) pointed
116 out that the brittle-ductile transition at the grain scale is also a function of the elastic properties and
117 therefore likely dependent on direction in strongly anisotropic materials.

118 Elastic properties, and anisotropy, is also known to influence the 'ductile' or plastic deformation of
119 minerals, and has a role in twinning, crystal plasticity (dislocation creep) and phase transformations
120 (e.g. Tullis, 1969; Christian & Mahajan, 1995; Timms et al., 2018). The role of mineral elasticity is
121 also important for inhomogeneous distribution of stresses at the grain scale necessary for driving
122 pressure solution creep, and is either treated implicitly (e.g., Wheeler, 1992) or explicitly (e.g.,
123 Wheeler, 2018). However, in many studies of rock deformation, minerals are commonly assumed to
124 be elastically isotropic and scalar mean values of elastic moduli are used, and/or elastic strains are
125 assumed to be small relative to plastic deformation and so ignored (e.g., in visco-plastic self-
126 consistent (VPSC) code) (Tomé & Lebensohn, 2014).



127 Given the key role that the elastic behavior of minerals plays in so many fundamental geological
128 processes, the scientific need to explore, understand and quantify directional variations in elastic
129 properties in minerals is clear, as is the need to develop better approaches to their graphical
130 visualisation. It is very difficult to full appreciate the variations in elastic properties of a mineral
131 simply by inspection of the 4th rank stiffness (or compliance) tensor, even in reduced form (Voigt
132 notation; see below). A related requirement is the ability to investigate the interactions of mineral
133 elastic anisotropy with imposed pressure, stress, or strain. However, the visualisation and full
134 appreciation of the properties of 2nd rank tensors, such as stress and strain, also presents challenges.
135 No single surface can simultaneously portray the full anisotropy quantified by the diagonal (normal)
136 and off-diagonal (shear) components of these tensorial mechanical quantities. Depictions of strain
137 (or stress) as ellipsoids using only the principal values as semi-axes fail to quantify the directional
138 variations in shear strain (or stress) and cannot easily show examples with mixed positive and
139 negative principal values. We believe there are clear educational benefits to alternative approaches
140 to visualising stress and strain, which students commonly find challenging, both conceptually and
141 from a 3-dimensional cognition perspective. For example, most geological textbooks either
142 illustrate stress or strain as ellipses/ellipsoids of the normal component only (with the limitations
143 described above), Mohr diagrams, or written out in matrix notation. Furthermore, a common
144 misnomer that some minerals are isotropic in material properties undoubtedly stems from the strong
145 emphasis on optical properties of minerals in most undergraduate mineralogy courses. Software
146 tools with the capability of comparative visualisation of various physical properties of minerals in
147 2- and 3-dimensions, including elastic, optical, and acoustic anisotropy have a valuable place in
148 teaching and learning in mineralogy and in scientific research.

149 While the number of published datasets for single mineral elastic anisotropy continues to increase,
150 there are relatively few publications that have reviewed or synthesised the available data. Gercek
151 (2007) provided a useful review of Poisson's ratio for rocks and included some data for specific
152 minerals. A more recent review of Poisson's ratio in rocks (Ji et al., 2018) also contained data for
153 minerals, but used their calculated Voigt-Reuss-Hill average values rather than quantify their
154 anisotropy. Workers in the fields of chemistry, physics and engineering have published methods
155 and tools for visualising the elastic anisotropy of various groups of solid elements and compounds
156 (Karki & Chennamsetty, 2006; Lethbridge et al., 2010; Marmier et al., 2010; Gaillac et al., 2016),
157 and these predominantly focus on Poisson's ratio. In earth sciences, the MTEX toolbox for the
158 analysis and modelling of crystallographic textures from electron backscatter diffraction (EBSD)
159 data provides stereographic projections of elastic properties, such as Young's modulus, for single
160 minerals (Hielscher, R. & Schaeben, H., 2008; Mainprice et al., 2011). The MSAT toolbox for
161 seismic anisotropy also contains options for plotting the elastic anisotropy of rocks and minerals
162 (Walker & Wookey, 2012). Both MTEX and MSAT provide one or more options for displaying
163 the elastic properties of minerals, but their main focus is on the analysis of textures and seismic
164 (acoustic) velocity anisotropy, respectively.

165 In this paper we present the AnisoVis toolbox, a collection of new MATLAB scripts based on
166 published methods with a graphical user interface (GUI), to explore the range of elastic anisotropy
167 displayed by rock forming minerals. Specifically, AnisoVis depicts the magnitude of the
168 directional variations in elastic properties such as Young's modulus (E), Poisson's ratio (ν), shear
169 modulus (G) and linear compressibility (β) using a range of 2- and 3-dimensional representations of
170 each elastic property to enable a complete assessment of the anisotropy in relation to the crystal



171 symmetry. We exploit the large database of published elastic constants for rock-forming minerals
172 to systematically assess the anisotropy of different elastic properties as a function of temperature
173 and pressure (where possible), giving new insights into the elastic behaviour of rock-forming
174 minerals. Most of the figures presented in this paper have been produced from the AnisoVis
175 toolbox, which is freely available on the web.

176 A table of symbols and terms used in this paper is provided in Table 1. We follow the geological
177 convention that compressive stress is positive, tensile stress is negative. Elastic properties are
178 reported in SI units. In Section 2 we review the theoretical basis of linear elasticity and the formal
179 description of elastic anisotropy in terms of the key equations. We then describe the methods we
180 use to visualise and quantify the directional variations in elastic properties for any given mineral.
181 We present two sets of results. Firstly, we analyse general trends in the database of 86 distinct
182 minerals with 246 separate elasticity datasets from published sources, and summarise the degree of
183 anisotropy to be found in rock forming minerals. Secondly, we analyse specific examples and focus
184 on their response to applied deformation. We review the key issues raised by these analyses in the
185 Summary. The Appendix contains benchmarks of the calculations performed in AnisoVis in
186 comparison to published output from previous workers.

Quantity	Symbol	Default SI unit
Young's modulus	E	Pa
Poisson's ratio	ν	
Shear modulus	G	Pa
Linear compressibility	β	Pa^{-1}
Bulk modulus	K	Pa
Compliance	s	Pa^{-1}
Stiffness	c	Pa
Stress	σ	Pa
Strain	ε	
Normal stress	σ_n	Pa
Shear stress	τ	Pa
Normal strain	ε_n	
Shear strain	γ	
Unit vectors parallel to crystallographic axes	a, b, c	Miller notation

187 **Table 1.** List of symbols and terms used in this paper, together with their default units (if any).



188

189 2. Theory and underlying equations

190 The elastic anisotropy of a solid material is described by a fourth rank tensor, either the compliance
191 s_{ijkl} or its inverse, the stiffness c_{ijkl} . For linear elastic deformation, the generalised form of Hooke's
192 Law can be written as:

$$193 \quad \varepsilon_{ij} = s_{ijkl} \sigma_{kl} \quad (1)$$

194 where ε_{ij} and σ_{ij} are the second rank tensors of strain and stress, respectively. Alternatively,
195 equation (1) can be written as:

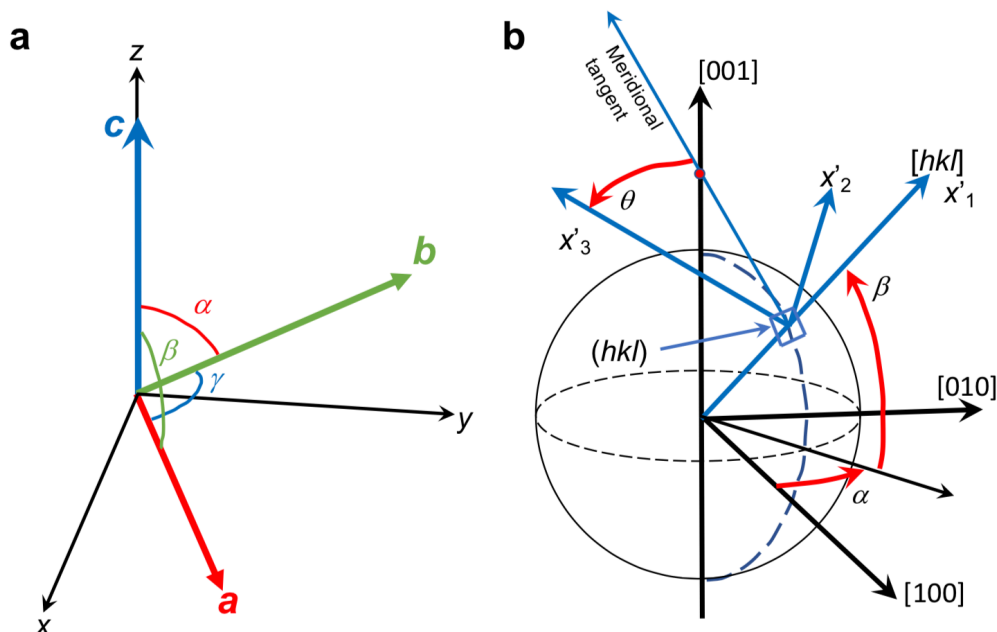
$$196 \quad \sigma_{ij} = c_{ijkl} \varepsilon_{kl} \quad (2).$$

197 Symmetry considerations lead to $s_{ijkl} = s_{ijlk}$ and $s_{ijkl} = s_{jikl}$ (Nye, 1985). The corollary of these
198 relationships is that the number of independent (potentially unique) components of s_{ijkl} is reduced
199 from 81 ($=3^4$) to 36. The same applies to c_{ijkl} . The elastic compliance s or stiffness c of a crystal
200 can therefore be represented in a more compact form, known as the Voigt matrix. This is a square 6
201 x 6 matrix where, for example, the elements of elastic stiffness are defined as $c_{IJ} = c_{ijkl}$, where $I = ij$
202 and $J = kl$. There are six different permutations of $I(J) = ij(kl)$, the details of which are listed in
203 Nye (1985) and more recently in Almqvist & Mainprice (2017).

204 The measured and calculated elastic properties of single crystals are reported in Voigt matrix
205 notation (s_{IJ} , c_{IJ}), where the indices $I, J (=1,2,3)$ relate to a standard Cartesian reference frame ($x=1$,
206 $y=2$, $z=3$). The relationship between any specific crystal lattice and this Cartesian reference is
207 arbitrary, but we adopt the convention described in Britton et al. (2016). In this system:

- 208 • the unit cell lattice vectors \mathbf{a} , \mathbf{b} , and \mathbf{c} form a right-handed set,
- 209 • \mathbf{c} is parallel to Cartesian z ,
- 210 • \mathbf{b} lies in the Cartesian y - z plane at angle α to \mathbf{c} , and
- 211 • \mathbf{a} is directed at angle β to \mathbf{c} and γ to \mathbf{b} .

212 Note that α is the angle between \mathbf{b} and \mathbf{c} , β is the angle between \mathbf{c} and \mathbf{a} and γ is the angle between
213 \mathbf{a} and \mathbf{b} (see Figure 1a).



214

215 **Figure 1.** a) Crystallographic orientation convention (after Britton et al., 2016) and b) geometrical
 216 reference frame (after Turley & Sines, 1971) used in this paper.

217 Familiar elastic properties, such as Young's modulus (E), Poisson's ratio (ν) and shear modulus
 218 (G), can be expressed directly in terms of the components of the compliance matrix. For example,
 219 the Young's modulus of a single crystal for a uniaxial stress applied in the x -direction is:

$$220 \quad E_x = E_I = 1 / s_{11} \quad (3)$$

221 and the Poisson's ratio for a uniaxial stress and axial strain along x and a lateral strain along y is

$$222 \quad \nu_{xy} = -s_{21} / s_{11} \quad (4)$$

223 Note that, in general for anisotropic materials, $\nu_{xy} \neq \nu_{yx}$ etc.

224 Guo & Wheeler (2006) note that although Poisson's ratio may be negative for some directions,
 225 these are often compensated by higher positive values in transverse directions perpendicular the
 226 minima in the same plane. They suggest a more useful measure of extreme auxeticity, the **areal**
 227 **Poisson's ratio**, defined as the average of all values of Poisson's ratio taken within the plane
 228 normal to a chosen direction. If the areal Poisson's ratio is negative this implies that a cylinder of
 229 the mineral would contract under a uniaxial compression, around the whole circumference, and not
 230 just along certain directions.

231 In order to calculate specific values of these elastic properties in more general directions within a
 232 crystal – i.e. not just along the axes of the default Cartesian reference frame – we need to transform
 233 the compliance matrix into a different reference frame. We follow the notation used by Turley &
 234 Sines (1971) based on Eulerian angles α , β and θ (see Figure 1b) that define the new Cartesian axes



235 $(1', 2', 3'$ or $x', y', z')$ in relation to the initial reference frame $(1, 2, 3$ or $x, y, z)$. The transformation
 236 of compliance matrix s_{ijkl} to s'_{ijkl} is given by (Nye, 1985):

$$237 \quad s'_{ijkl} = a_{im} a_{jn} a_{ko} a_{lp} s_{mnop} \quad (5)$$

238 where the elements of the rotation matrix \mathbf{a} are given by:

$$239 \quad a_{ij} = \begin{bmatrix} A & B & C \\ (D \sin \theta + E \cos \theta) & (F \sin \theta + G \cos \theta) & H \sin \theta \\ (D \cos \theta - E \sin \theta) & (F \cos \theta - G \sin \theta) & H \cos \theta \end{bmatrix} \quad (6)$$

240 where $A = \cos \alpha \cos \beta$, $B = \sin \alpha \cos \beta$, $C = \sin \beta$, $D = -\cos \alpha \sin \beta$, $E = -\sin \alpha$, $F =$
 241 $-\sin \alpha \sin \beta$, $G = \cos \alpha$, $H = \cos \beta$ (Turley & Sines, 1971).

242 Using the transformed compliance matrix s'_{ijkl} , we can now calculate the elastic properties for any
 243 general direction within the crystal defined by a unit vector with angles α , β and θ , for example:

$$244 \quad E'_{11} = 1 / s'_{11} \quad (7)$$

$$245 \quad G'_{12} = 1 / s'_{66} \quad (8)$$

$$246 \quad \nu'_{12} = -s'_{21} / s'_{11} \quad (9)$$

247 To calculate the variation in any elastic property over all possible directions in 3D, we simply need
 248 to vary α and β over a unit sphere (α : 0-360°, β : 0-180°) and vary θ over a unit circle (θ : 0-360°).

249 *Isotropic approximations of anisotropic elastic properties*

250 Two useful ‘averaging’ schemes that can be applied to the full set of anisotropic elastic properties
 251 of polycrystals are those due to Reuss and Voigt (see Hill, 1952). The bulk and shear moduli in the
 252 Voigt scheme are defined as:

$$253 \quad K^V = [(c_{11} + c_{22} + c_{33}) + 2(c_{12} + c_{23} + c_{31})]/9 \quad (10)$$

$$254 \quad G^V = [(c_{11} + c_{22} + c_{33}) - (c_{12} + c_{23} + c_{31}) + 3(c_{44} + c_{55} + c_{66})]/15 \quad (11)$$

255 and in the Reuss scheme as:

$$256 \quad K^R = 1/[(s_{11} + s_{22} + s_{33}) + 2(s_{12} + s_{23} + s_{31})] \quad (12)$$

$$257 \quad G^R = 15/[4(s_{11} + s_{22} + s_{33}) - 4(s_{12} + s_{23} + s_{31}) + 3(s_{44} + s_{55} + s_{66})] \quad (13)$$

258 The Voigt average of any property always exceeds the Reuss average and the ‘true’ value lies
 259 somewhere in between. The Voigt-Reuss-Hill (VRH) average of a property is defined as the
 260 arithmetic mean of the Voigt and Reuss estimates e.g. $G^{VRH} = (G^V + G^R)/2$. Note that, although only
 261 formally defined for polycrystals and based on averaging over many grains, the Voigt, Reuss and
 262 VRH estimates are in practice useful for single crystals: if we consider a polycrystal made of many
 263 grains all aligned perfectly parallel, then the elastic anisotropy of this polycrystal is identical to that
 264 of the single crystal.



265 To plot the variations of disparate elastic properties across minerals with widely different
266 symmetries and anisotropies, we use the Universal Anisotropy Index (A^U), of Ranganathan &
267 Ostoja-Starzewski (2008), defined as:

$$268 \quad A^U = 5 \frac{G^V}{G^R} + \frac{K^V}{K^R} - 6 \quad (14)$$

269 where G^V and K^V are the Voigt average shear and bulk moduli, respectively; and G^R and K^R are the
270 Reuss average shear and bulk moduli, respectively.

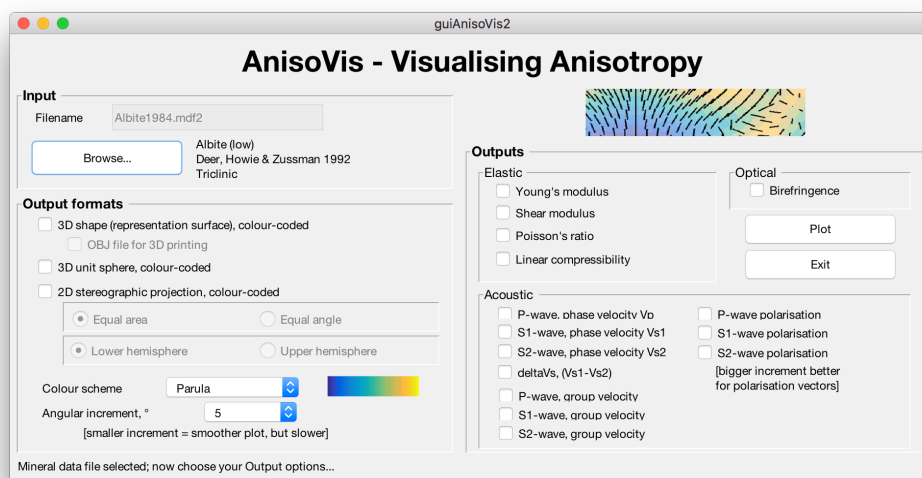
271

272 **3. AnisoVis – program description and visualisation methods**

273 The visualisations of elastic anisotropy presented in this paper have been prepared using AnisoVis,
274 a set of custom scripts linked to a graphical user interface (GUI) and written in MATLAB™. This
275 code is available as an open source project on GitHub (link) and through the MathWorks™
276 FileExchange server (link). Single mineral elasticity values are supplied as input data, together
277 with lattice parameters defining the unit cell and symmetry. The code then calculates the
278 directional variations in elastic properties and produces outputs of the kinds shown in Figures 4-7.
279 AnisoVis can also calculate the acoustic velocities (phase and group) and their polarisations, and
280 the optical birefringence from the refractive indices. Over 240 data files for 86 different minerals
281 are included (from published sources), and a user guide is provided with the software.

282 *Installation and input file format*

283 AnisoVis is installed by copying all of the files from the GitHub or Mathworks FileExchange server
284 into a folder on the user's computer. AnisoVis will run on any computer with MATLAB installed,
285 including running Windows, Mac OS X or different versions of Linux. After starting MATLAB,
286 the working folder or directory should be set to the folder containing all of the installed source
287 code. The application is started by typing 'AnisoVis' in the Command window of the MATLAB
288 session. There is only one window in AnisoVis (Figure 2). Click 'Browse...' to show the standard
289 dialog to open an input file of mineral properties. These are stored in formatted tab-delimited
290 ASCII text files with an extension of '.mdf2' ('mineral data file'). The user guide supplied with the
291 software has examples for each different mineral symmetry class.



292

293 **Figure 2.** The graphical user interface in AnisoVis, showing the range of output options for elastic
294 (and acoustic and optical) anisotropies.

295 *Calculations*

296 After selecting the required output formats (shape, sphere or stereogram) and anisotropic properties
297 to be visualised (elastic, acoustic or optical), the user clicks Plot to generate the images.
298 Calculations are performed using the equations for each property described above, looping through
299 three-dimensional space with the specified angular increment. Smaller angular increments (e.g. 1-
300 2°) take longer to run than larger increments (e.g. 5-10°). In the tests that we have conducted to
301 date, run time has been very satisfactory, with most operations completed in a few seconds on
302 standard desktop computers purchased within the last three years. The exception to this
303 performance is when the angular increment is 1°, where run times are typically of the order of 1-2
304 minutes. We have implemented a MATLAB™ WaitBar to provide basic progress information for
305 lengthier tasks.

306 *Generating outputs*

307 Output is directed to MATLAB figure windows, with one plotted property per figure window.
308 These images are automatically saved as '.tif' files at 600 dpi resolution in the working folder.
309 While each figure window is visible, the user can exploit standard MATLAB functionality to resize
310 or reformat the figure as they wish, and can save the figure to a different filename or folder, or even
311 a different graphic format (e.g. '.png' or '.jpeg'). The colour schemes used for the representation
312 surfaces, unit spheres and stereograms can be varied using the drop-down list box in the main
313 window. In addition to the standard MATLAB colour map of 'Parula' we offer 3 other choices
314 from the cmocean colour map library (Thyng et al., 2016) using perceptually uniform scales
315 ('Haline', 'Thermal' and 'Matter').

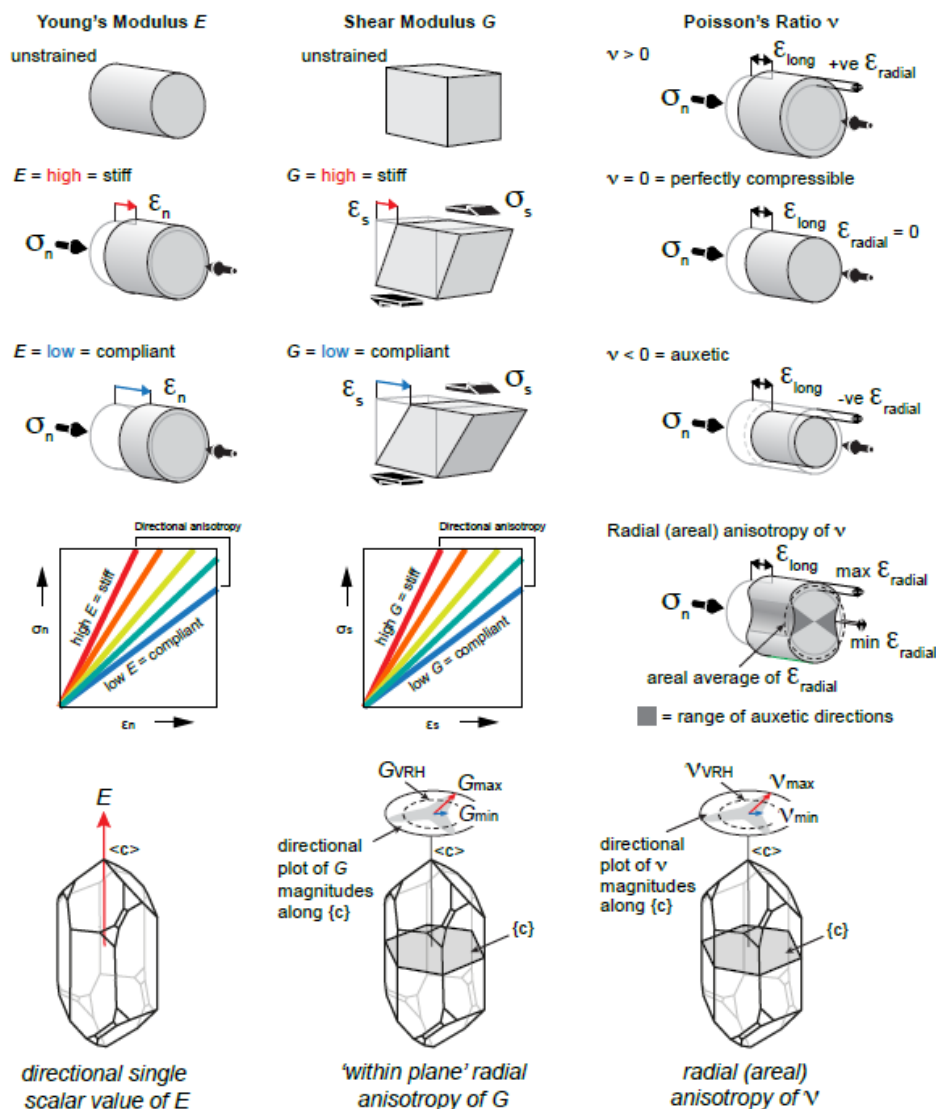
316 *Visualising elastic anisotropy in 2-D and 3-D*



317 As pointed out by Nye (1985), no *single* surface can represent the elastic behaviour of a crystal
318 completely. However, we can plot specific surfaces that are useful in practice. To visualise the
319 anisotropy of elastic properties of single crystals we use a mixture of 3D surfaces and 2D polar
320 plots projected onto selected planes. We use representation surfaces (Nye, 1985) to generate 3D
321 shapes where, for any given radius vector measured from the origin to the surface, the radius is
322 proportional to the magnitude of the property in that direction. The magnitude of the property is
323 also conveyed by a colour mapping applied to the surface. An alternative method is to plot the
324 directional variation of a property projected onto a unit sphere, using a colour map to depict the
325 magnitude. We can also use stereographic projections (lower hemisphere, equal area) to show
326 directional variations in properties. Lastly, we can use polar plots to the variation of a property in
327 selected crystallographic planes (e.g. [100], [010], [001]).

328 *Challenges in visualising Poisson's ratio (ν) and shear modulus G*

329 Any of the above methods of visualisation can be used for 'simple' elastic properties, such as
330 Young's modulus or linear compressibility, where the property is a single scalar value for a given
331 direction. Young's modulus is defined as the ratio of uniaxial stress to uniaxial strain and it is
332 implicit that the directions of applied stress and measured strain are coincident (i.e. coaxial; Figure
333 3). However, for Poisson's ratio and shear modulus this is no longer the case. Poisson's ratio is
334 defined as the ratio of (negative) lateral strain to the axial strain, and therefore involves two
335 orthogonal directions (Figure 3). Shear modulus is defined as the ratio of the shear stress to the
336 shear strain, again involving two orthogonal directions (see Figure 3). For a stress (normal or
337 shear) applied in a specific direction, there is only one value of E , but there are many possible
338 values of ν and G . It can be seen from Figure 3 that ν and G will vary according to the direction of
339 the normal to the chosen direction $[hkl]$, described by angle θ in the Turley & Sines (1971) notation.
340 To plot representation surfaces for ν and G , we take their minimum and maximum values calculated
341 over θ for an applied stress along each direction in 3D-space. In addition, as ν can be negative for
342 some directions in some minerals, we further separate the minimum representation surfaces of
343 Poisson's ratio into negative minimum and positive minimum components where appropriate.

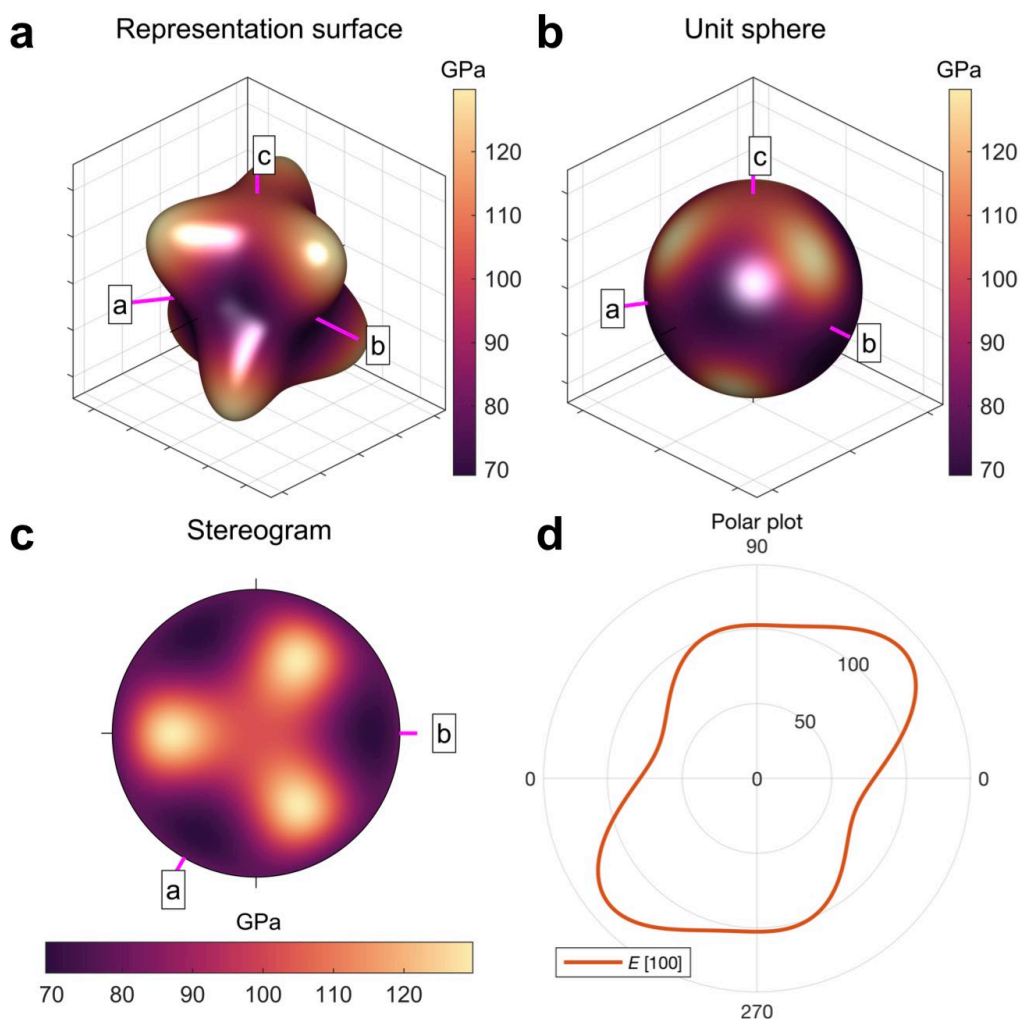


344

345 **Figure 3.** Schematic diagrams to illustrate the definitions of Young's modulus, Poisson's ratio,
 346 shear modulus in a 3D crystallographic reference frame, using α -quartz (trigonal) as an example.

347 *Example: α -quartz (trigonal; Ogi et al., 2006)*

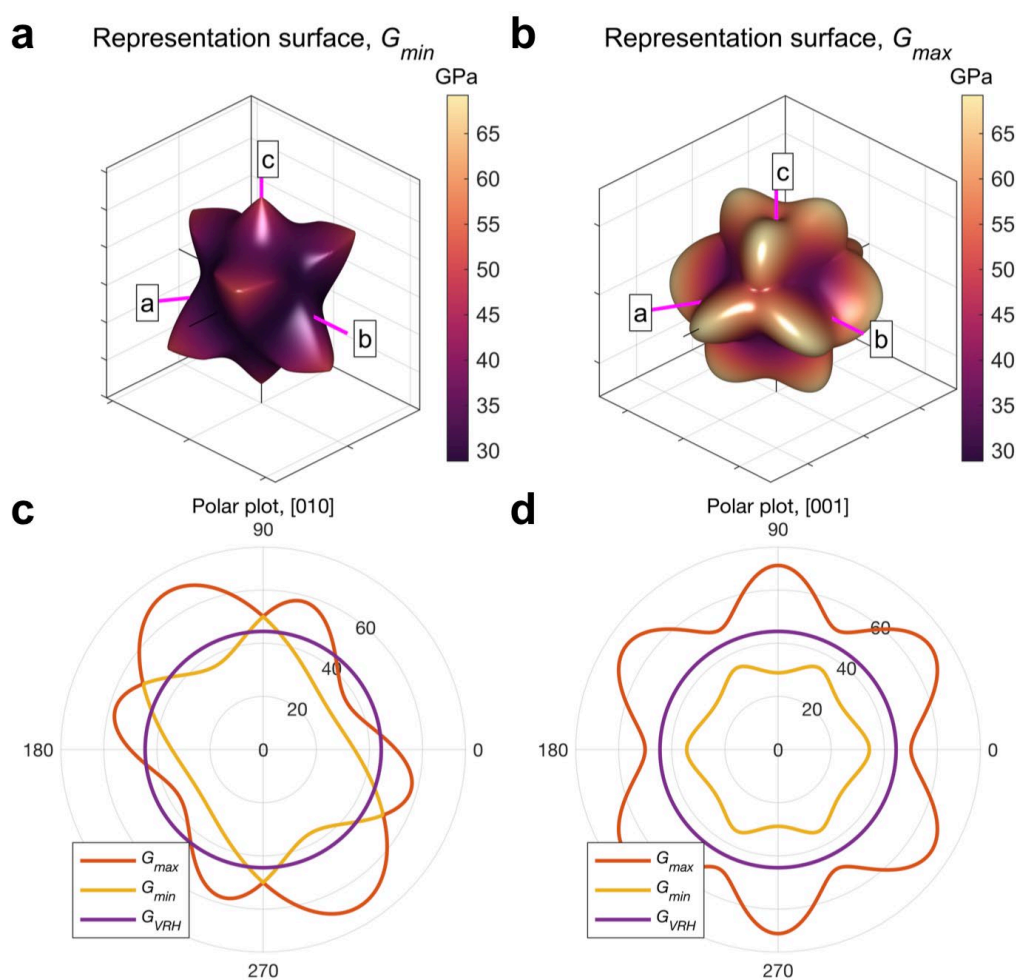
348 To illustrate the different possibilities described above we use the elasticity of α -quartz as
 349 quantified by Ogi et al. (2006). The anisotropy of Young's modulus is shown in Figure 4 using a
 350 representation surface, a unit sphere, a stereogram and polar plots of E in the plane (100). The
 351 colour bar scale is the same in all plots for ease of comparison. Using AnisoVis, the user can rotate
 352 any of these plot views in the MATLAB figures to gain a better appreciation of the directional
 353 variations in relation to the crystallographic reference axes $\langle a \rangle$, $\langle b \rangle$, and $\langle c \rangle$.



354

355 **Figure 4.** Alternative visualisations of the anisotropy of Young's modulus (E , in GPa) of α -quartz.
356 **a)** 3D representation surface where the radius in any direction is proportional to the magnitude of E .
357 **b)** Projection of E on to a unit sphere, colour coded by magnitude. **c)** Lower hemisphere, equal area
358 stereographic projection. **d)** Polar plot of anisotropy of E in the $[010]$ plane. Crystallographic axes
359 $\langle a \rangle$, $\langle b \rangle$, and $\langle c \rangle$ shown in pink. VRH = Voigt-Reuss-Hill average value of E .

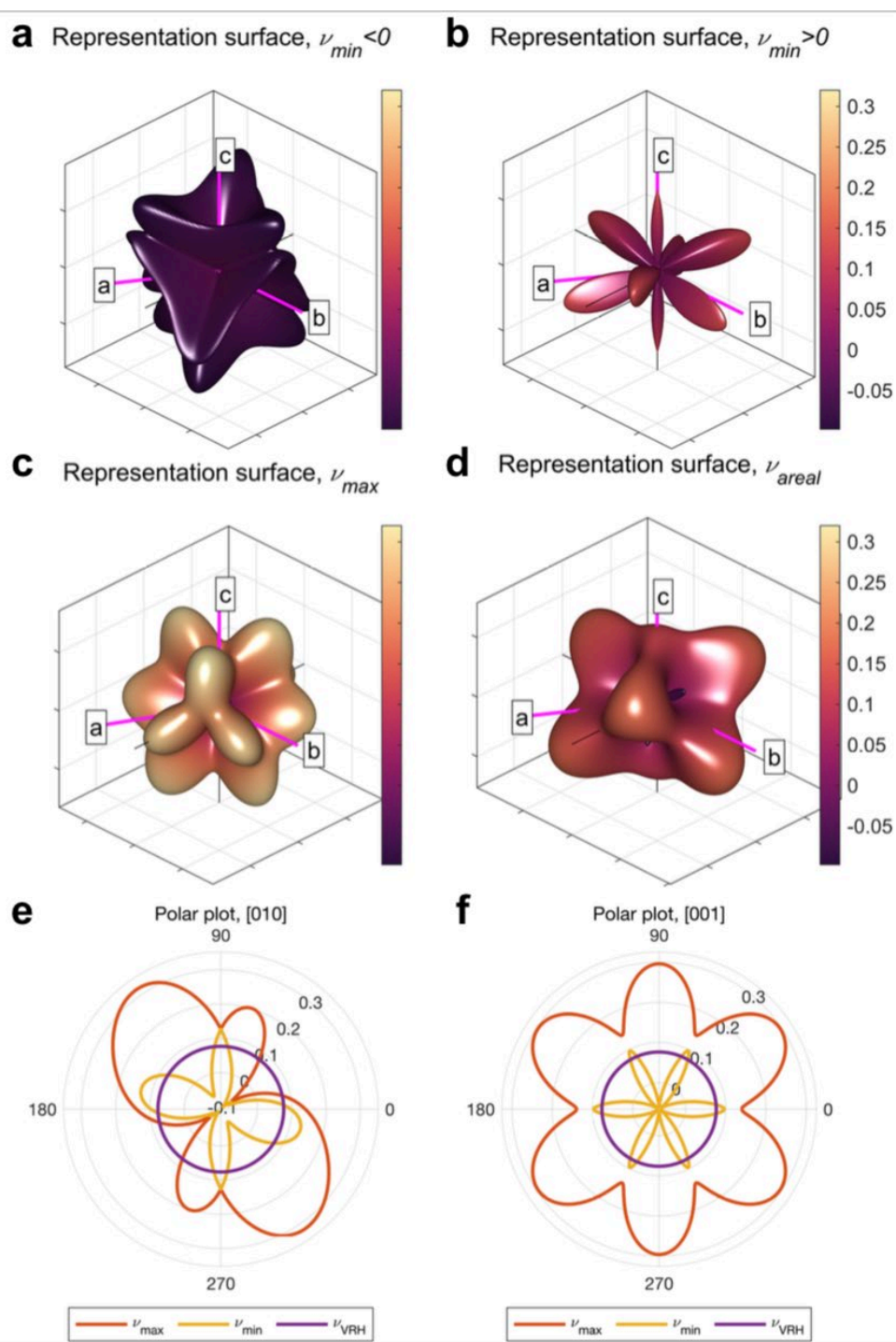
360 As noted above, the shear modulus is a function of shear stress in one direction and a shear strain in
361 a perpendicular direction. Therefore, for any given crystallographic direction in 3D space $[hkl]$ in
362 an anisotropic crystal there are many possible values of G as the transverse component is rotated
363 through the angle θ (see Figure 1b). In Figure 5 we show representation surfaces for the minimum
364 and maximum values of G of α -quartz associated with each direction $[hkl]$. Polar plots are also
365 shown for (010) and (001) .



366

367 **Figure 5.** Alternative visualisations of the anisotropy of shear modulus (G , GPa) of α -quartz. **a-b)**
368 3D representation surfaces where the radius in any direction is proportional to the magnitude of G .
369 Separate surfaces shown for minimum and maximum G . **c-d)** Polar plots of anisotropy of G in the
370 $[010]$ and $[001]$ planes, respectively. Crystallographic axes $\langle a \rangle$, $\langle b \rangle$, and $\langle c \rangle$ shown in pink. VRH
371 = Voigt-Reuss-Hill average value of G .

372 Visualising the directional variation of Poisson's ratio ν can pose further challenges. α -quartz is
373 auxetic and has many directions that show negative Poisson's ratios. As for shear modulus, we
374 show representation surfaces for both the minimum (Figure 6a-b) and maximum (Figure 6c)
375 Poisson's ratios, but we separate the minimum Poisson's ratio plot into two surfaces: one for $\nu_{\min} <$
376 0 (Figure 6a) and one for $\nu_{\min} > 0$ (Figure 6b). We also include a plot for the areal Poisson's ratio –
377 the value of Poisson's ratio averaged over all θ for each direction $[hkl]$ (Figure 6d, after Guo &
378 Wheeler, 2006). Polar plots for specific 2D planes can also be useful (Figure 6e-f).



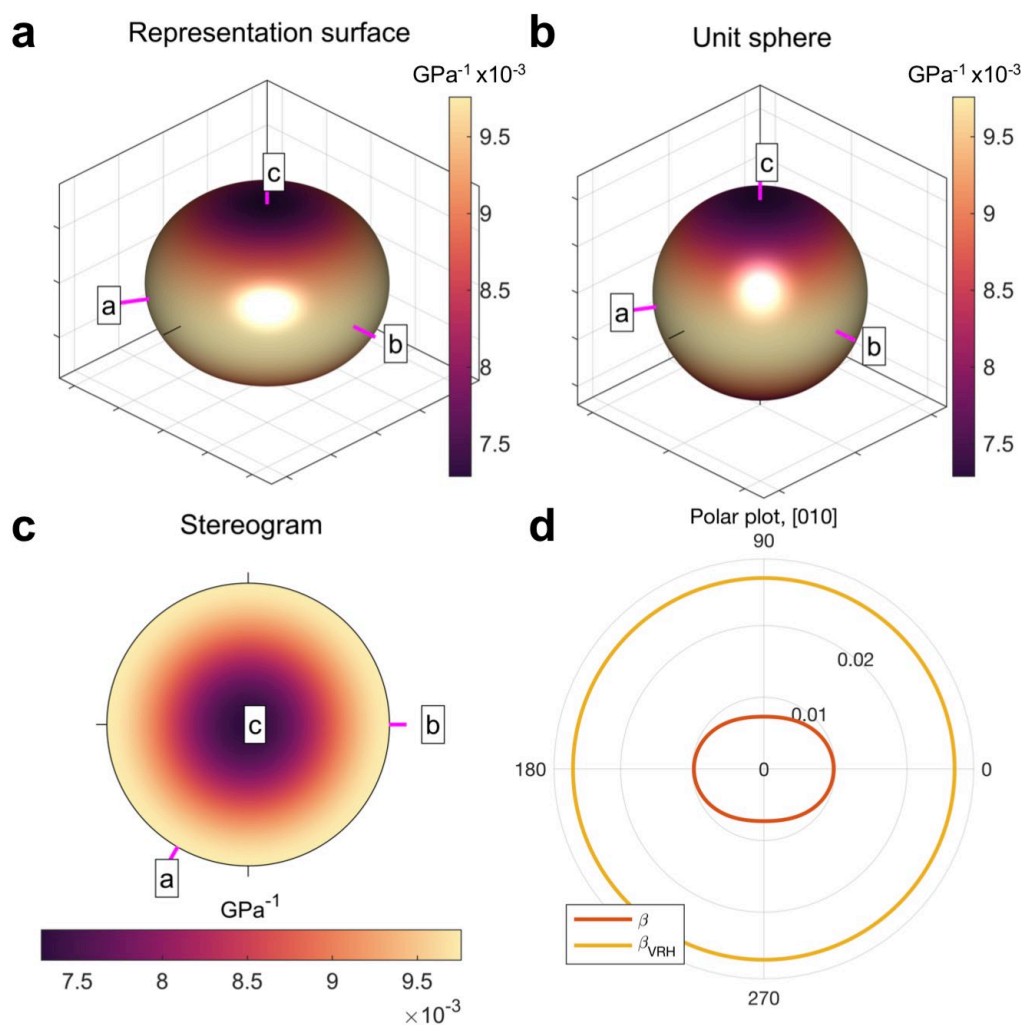
379

380 **Figure 6.** Alternative visualisations of the anisotropy of Poisson's ratio (ν) of α -quartz. **a-d)** 3D
 381 representation surfaces where the radius in any direction is proportional to the magnitude of ν .
 382 Separate surfaces shown for minimum negative, minimum positive, maximum and areal n , as



383 defined in the equations in Section N.N. **e-f**) Polar plots of anisotropy of ν in the [010] and [001]
384 planes, with separate lines shown for ν_{\min} , ν_{\max} and ν_{VRH} . Crystallographic axes $\langle a \rangle$, $\langle b \rangle$, and $\langle c \rangle$
385 shown in pink. VRH = Voigt-Reuss-Hill average value of ν .

386



387

388 **Figure 7.** Alternative visualisations of the anisotropy of linear compressibility (β , in GPa^{-1}) of α -
389 quartz. **a**) 3D representation surface where the radius in any direction is proportional to the
390 magnitude of β . **b**) Projection of β on to a unit sphere, colour coded by magnitude. **c**) Lower
391 hemisphere, equal area stereographic projection. **d**) Polar plot of anisotropy of β in the [010] plane.
392 Crystallographic axes $\langle a \rangle$, $\langle b \rangle$, and $\langle c \rangle$ shown in pink. VRH = Voigt-Reuss-Hill average value of
393 β .

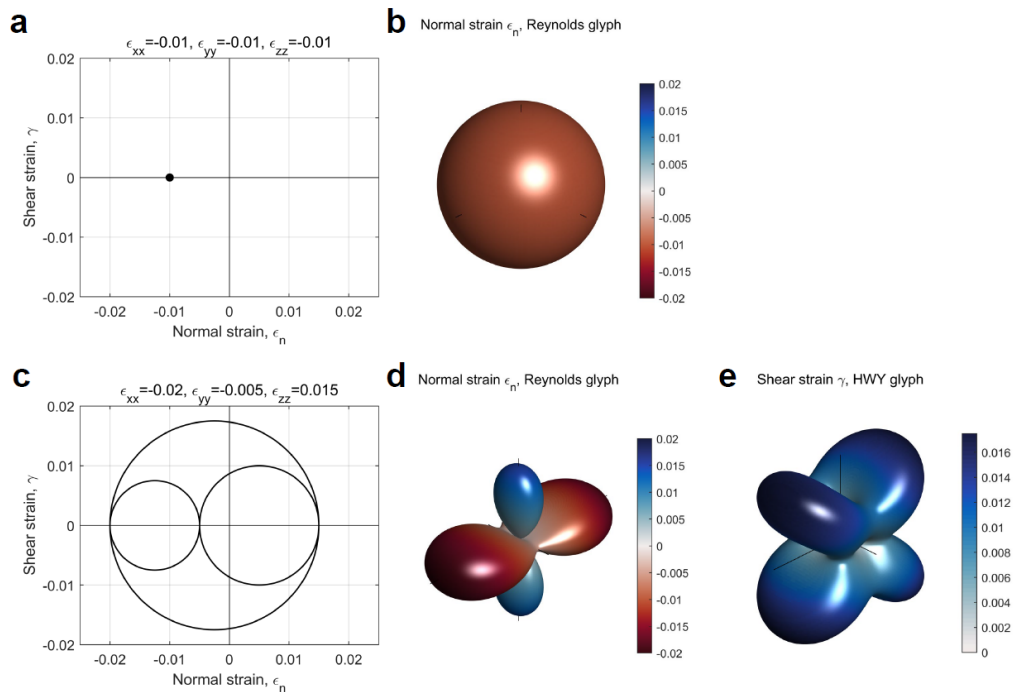
394 The linear compressibility (β) of an anisotropic crystal quantifies the directional response to an
395 applied hydrostatic load i.e. to pressure, not stress. For isotropic materials, the compressibility is a



396 scalar – directionally invariant – and is simply the inverse of the bulk modulus K ($\beta = 1 / K$). For
397 anisotropic rock forming minerals, this is no longer the case and β varies with direction. Figure 7
398 shows the variation for α -quartz using the same types of plots as for Young's modulus (Figure 5).
399 In summary, we note that as a corollary of the point made by Nye (1985) that no single surface can
400 represent the full richness of the 4th rank elasticity tensor, neither can any one measure (e.g. E , G , ν
401 or β) convey the complete behavior of an anisotropic mineral. The anisotropies of the different
402 parameters (through these plots) should be used in combination to understand a specific problem.

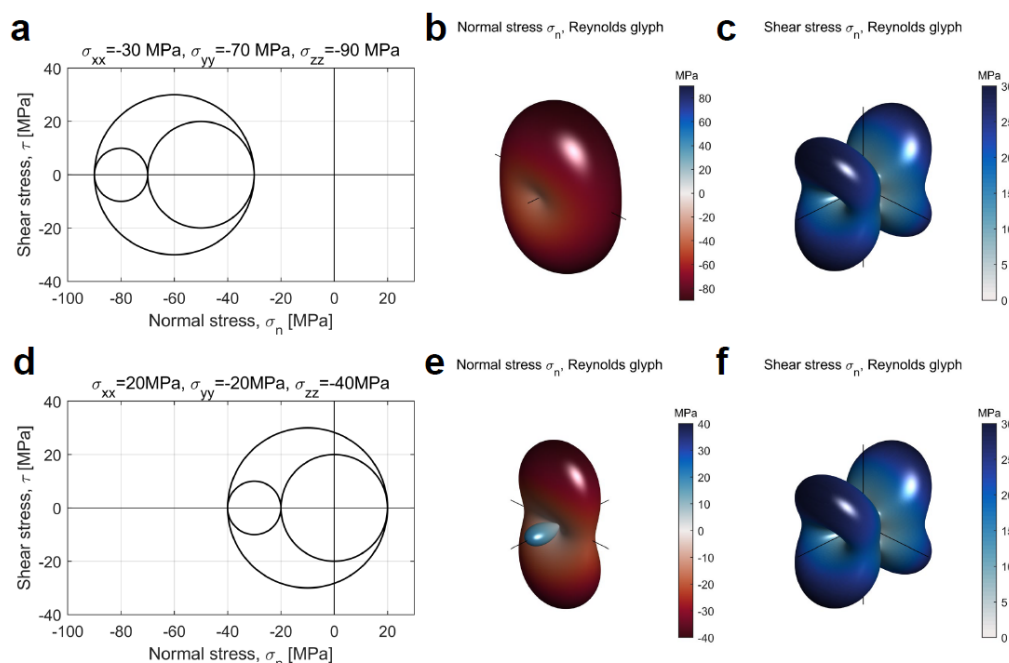
403 *Visualising second-rank tensors: stress and strain*

404 To address the challenges in visualizing stress and strain described above, we use two separate
405 graphical depictions, or glyphs, for the normal and shear components of the strain and stress tensors
406 (Kratz et al., 2014). We use the Reynolds glyph for normal strains and stresses, as this can show
407 positive and negative principal values (Moore et al., 1996). We use the HWY glyph to visualise the
408 shear components of the strain and stress tensors (Hashash et al., 2003). Figures 8 and 9 show
409 examples of the Reynolds and HWY glyphs for strains and stresses, respectively. Isotropic
410 compaction plots as a single point in Mohr space (Figure 8a), and as a sphere using a Reynolds
411 glyph (Figure 8b; shear strains are zero and so there is no HWY glyph). For a general triaxial strain
412 with both shortening and stretching components, the Reynolds and HWY glyphs are shown in
413 Figure 8d and 8e. Note that in the HWY glyph for shear strain the maxima are located at 45° to the
414 principal axes, and the minima (0) are located along the principal axes. Triaxially compressive
415 stress is shown in Figure 9a-c. Again, maxima of shear stress in the HWY glyph are at 45° to the
416 directions of the principal (normal) stresses. For a general triaxial stress with components of
417 compression and tension, the directional variations of normal and shear stress are shown in Figure
418 9d-f.



419

420 **Figure 8.** Examples of strain tensors depicted in Mohr space (ϵ_n , γ), and as Reynolds (normal
421 strains, ϵ_n) and HWY (shear strains, γ) glyphs. **a-b** Isotropic compaction (taken as negative, blue
422 colour). **c-e** Visualisations for a general triaxial strain. Note the lobes of extensional (blue) and
423 contractional (red) strain in the normal strain plot (d).



424

425 **Figure 9.** Examples of stress tensors depicted in Mohr space (σ_n , τ) and as Reynolds (normal stress,
426 σ_n) and HWY (shear stress, τ) glyphs. **a-c)** Triaxial compression (taken as negative, blue colour).
427 **d-f)** General triaxial stress with one principal stress tensile (σ_{xx}).

428 *Data sources*

429 The elastic properties of the minerals used in this study have been derived from previous
430 compilations and original sources where possible. Many compilations of elastic and other physical
431 properties are now available: see Bass (1995) and Almqvist & Mainprice (2017), and references
432 therein. Note that most elastic properties are measured by laboratory methods whereas a minority
433 are calculated from theory (*ab initio*). Single mineral lattice parameters have been extracted from
434 the same publication as the elasticity data where possible, but if this was not available, we took
435 representative values from Deer, Howie & Zussman (1992).

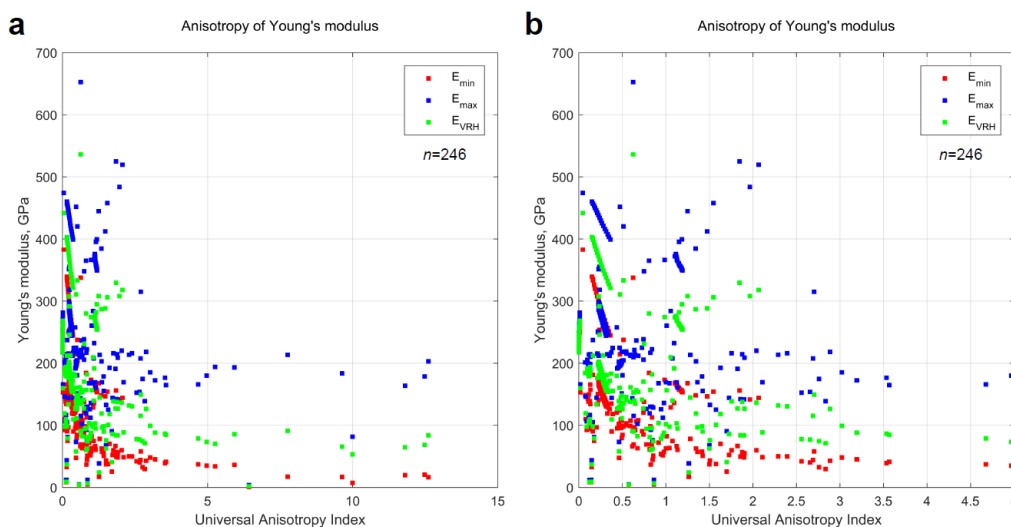
436

437 **4. Results – General trends**

438 From our database of published elastic properties of rock-forming minerals (246 data files covering
439 86 distinct minerals, all included with AnisoVis), we have calculated the maxima and minima for
440 Young's modulus, Poisson's ratio, shear modulus and linear compressibility. In Figure 10 we show
441 the variation in the anisotropy of Young's modulus (E) for 246 rock forming minerals as a function
442 of A^U . If we consider a simple measure of the anisotropy of E as the ratio between the maximum
443 and minimum values, it is clear that most minerals display significant anisotropy with E_{max}/E_{min}
444 often greater than 2. With increasing A^U , many minerals show E_{max}/E_{min} ratios of about 4. Figure
445 11 shows the anisotropy of shear modulus (G) for the same rock forming minerals, plotted against

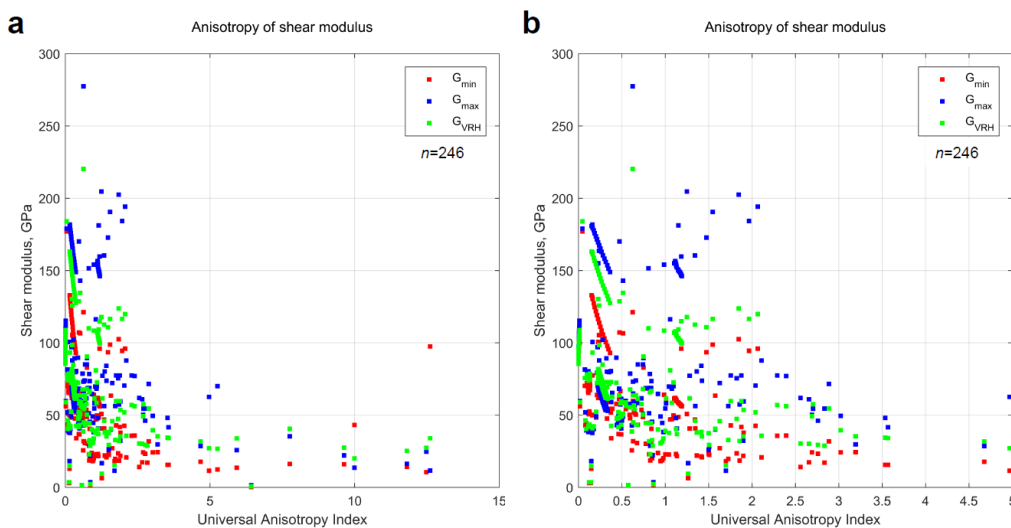


446 A^U . The anisotropy of G , simply defined as G_{max}/G_{min} , is less than that shown for E , and there is a
447 general pattern of decreasing anisotropy of G with increasing A^U .



448
449 **Figure 10.** Anisotropy of Young's modulus in rock-forming minerals ($n=246$) plotted against the
450 Universal Anisotropy Index (A^U) of Ranganathan & Ostoja-Starzewski (2008). E_{VRH} is the Voigt-
451 Reuss-Hill average of E . Many minerals display anisotropy of E (E_{max}/E_{min}) of 2 or more. **b)** Close-
452 up of data in **a)** for UA Index up to 5.

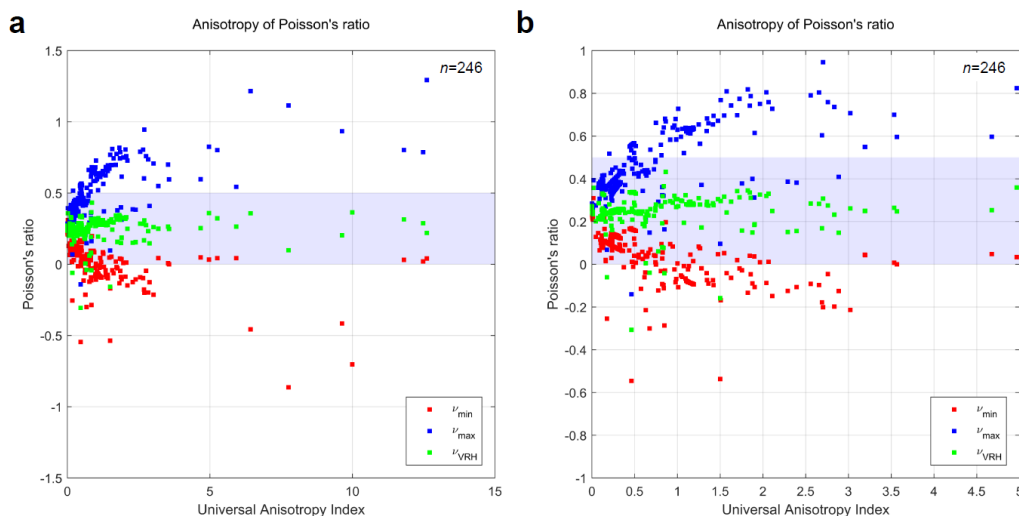
453



454
455 **Figure 11.** Anisotropy of shear modulus in rock-forming minerals ($n=246$) plotted against the
456 Universal Anisotropy Index of Ranganathan & Ostoja-Starzewski (2008). G_{VRH} is the Voigt-Reuss-
457 Hill average of G . **b)** Close up of data in **a)** for UA Index up to 5.

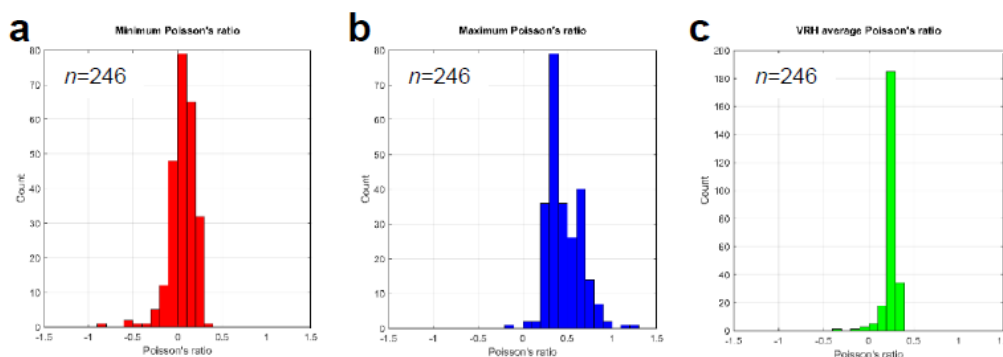


458 Figure 12 shows the variation in Poisson's ratio (ν) versus A^U for all minerals. The shaded area in
 459 Figure 12a and 12b denotes the range $0 \leq \nu \leq 0.5$. As noted by Ting & Chen (2005), ν for
 460 anisotropic materials can have no bounds. The data show that many minerals have minimum values
 461 less than 0 and maximum values greater than 0.5. The histogram in Figure 13 shows the statistical
 462 variation in ν_{min} for all minerals: 28% (=70/246) have negative minimum values for Poisson's ratio
 463 – that is, they display auxetic behaviour. Analysis of the variation of ν_{max} shows that 37%
 464 (=91/246) have values greater than 0.5 (Figure 13b). The mean value of the Voigt-Reuss-Hill
 465 average of Poisson's ratio for all minerals is 0.2464 (Figure 13c), close to the default assumption of
 466 many simplifications to elastic isotropy ($\nu=0.25$). A full list of the rock forming minerals in our
 467 database that show auxetic behaviour is shown in Table 2, and the specific directions of negative ν
 468 are shown for several examples in the stereograms in Figure 14.



469 **Figure 12.** a) Anisotropy of Poisson's ratio in rock-forming minerals (n=246) plotted against the
 470 Universal Anisotropy Index of Ranganathan & Ostoja-Starzewski (2008). ν_{VRH} is the Voigt-Reuss-
 471 Hill average of ν . b) Close up of data in a) for UAI up to 5.

473



474 **Figure 13.** a) Histogram of ν_{min} values shown in Figure 12. Note that 28% (n=70/246) of minerals
 475



476 display negative ν_{\min} . **b)** Histogram of ν_{\max} values. 37% (n=91/246) minerals display $\nu_{\max} > 0.5$. **c)**
 477 Histogram of ν_{VRH} values. Mean $\nu_{\text{VRH}} = 0.2464$, very close to the common default assumption of ν
 478 = 0.25.
 479

Mineral	Symmetry	Minimum $\nu < 0$	Minimum areal $\nu < 0$	Reference	
Albite (An0)	Triclinic	-0.03		Hearmon, 1984	
	Triclinic	-0.15		Brown et al., 2016	
Anhydrite	Orthorhombic	-0.046		Hearmon, 1979	
Andesine (An37)	Triclinic	-0.091		Brown et al., 2016	
Andesine (An48)	Triclinic	-0.075		Brown et al., 2016	
Antigorite	Monoclinic	-0.215		Bezacier et al., 2010	
Aragonite	Orthorhombic	-0.061		Hearmon, 1979	
Augite	Monoclinic	-0.012		Alexandrov et al., 1964	
Bytownite (An78)	Triclinic	-0.053		Brown et al., 2016	
Calcite	Trigonal	-0.047		Babuska & Cara, 1991	
	Hexagonal	-0.02		Chen et al., 2001	
Coesite	Monoclinic	-0.108		Weidner & Carleton, 1977	
α -Cristobalite	Tetragonal	-0.537	-0.262	Pabst & Gregorova, 2013	
β -Cristobalite	Cubic	-0.288	-0.162	Pabst & Gregorova, 2013	
Dolomite	Trigonal	-0.064		Hearmon, 1979	
Hornblende	Monoclinic	-0.075		Hearmon, 1984	
Illite-Smectite	Monoclinic	-0.416		Militzer et al., 2011	
Labradorite	Triclinic	-0.085		Ryzhova, 1964	
Labradorite (An60)	Triclinic	-0.009		Brown et al., 2016	
Labradorite (An67)	Triclinic	-0.025		Brown et al., 2016	
Lawsonite	Orthorhombic	-0.088		Sinogeikin et al., 2000	
Microcline	Triclinic	-0.199	-0.042	Babuska & Cara, 1991	
Oligoclase (An25)	Triclinic	-0.098		Brown et al., 2016	
Orthoclase	Monoclinic	-0.169		Hearmon, 1984	
	Monoclinic	-0.092		Waesermann et al., 2016	
α -Quartz	Trigonal	-0.97	-0.071	Ogi et al., 2006	
		-0.93	-0.067	Babuska & Cara, 1991	
	T=200°C	Trigonal	-0.123	-0.088	Lakshtanov et al., 2007
	T=400°C	Trigonal	-0.215	-0.138	Lakshtanov et al., 2007
	T=500°C	Trigonal	-0.301	-0.186	Lakshtanov et al., 2007
	T=573°C	Trigonal	-0.546	-0.398	Lakshtanov et al., 2007
	T=575°C	Hexagonal	-0.255	-0.095	Lakshtanov et al., 2007
Rutile	Tetragonal	-0.044		Manghnani, 1969	
Sanidine	Monoclinic	-0.097		Waesermann et al., 2016	
Sillimanite	Orthorhombic	-0.001		Verma, 1960	
Sphalerite	Cubic	-0.025		Hearmon, 1984	
Spinel	Cubic	-0.07		Hearmon, 1984	

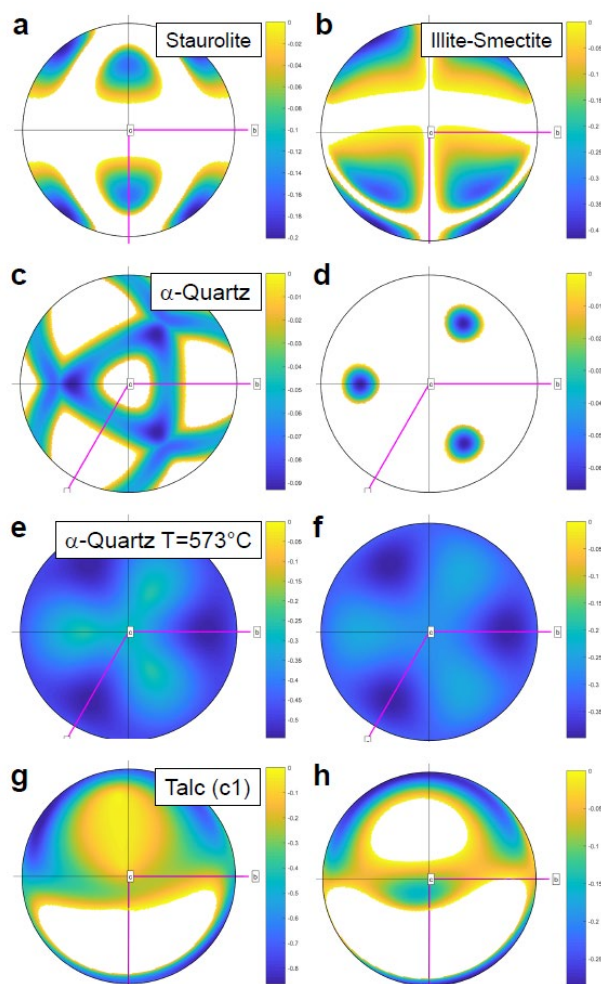


T=300°K	Cubic	-0.081		Anderson & Isaak, 1995
T=350°K	Cubic	-0.079		Anderson & Isaak, 1995
T=400°K	Cubic	-0.083		Anderson & Isaak, 1995
T=450°K	Cubic	-0.083		Anderson & Isaak, 1995
T=500°K	Cubic	-0.084		Anderson & Isaak, 1995
T=550°K	Cubic	-0.084		Anderson & Isaak, 1995
T=600°K	Cubic	-0.085		Anderson & Isaak, 1995
T=650°K	Cubic	-0.033		Anderson & Isaak, 1995
T=700°K	Cubic	-0.088		Anderson & Isaak, 1995
T=750°K	Cubic	-0.089		Anderson & Isaak, 1995
T=800°K	Cubic	-0.09		Anderson & Isaak, 1995
T=850°K	Cubic	-0.092		Anderson & Isaak, 1995
T=900°K	Cubic	-0.093		Anderson & Isaak, 1995
T=950°K	Cubic	-0.094		Anderson & Isaak, 1995
T=1000°K	Cubic	-0.095		Anderson & Isaak, 1995
Staurolite	Orthorhombic	-0.201		Hearmon, 1979
Stishovite	Tetragonal	-0.04		Babuska & Cara, 1991
Talc (c1)	Triclinic	-0.864	-0.287	Mainprice et al., 2008
P=0.87 GPa	Triclinic	-0.178	-0.001	Mainprice et al., 2008
P=1.96 GPa	Triclinic	-0.107		Mainprice et al., 2008
P=3.89 GPa	Triclinic	-0.009		Mainprice et al., 2008
Talc (c2c)	Monoclinic	-0.126	-0.029	Mainprice et al., 2008
P=0.15 GPa	Monoclinic	-0.107	-0.021	Mainprice et al., 2008
P=0.35 GPa	Monoclinic	-0.125	-0.025	Mainprice et al., 2008
P=0.64 GPa	Monoclinic	-0.091	-0.002	Mainprice et al., 2008
P=0.93 GPa	Monoclinic	-0.028		Mainprice et al., 2008
P=1.72 GPa	Monoclinic	-0.019		Mainprice et al., 2008
Zircon (metamict)	Tetragonal	-0.113		Hearmon, 1984
Zoisite	Orthorhombic	-0.014		Mao et al., 2007
Number of distinct minerals		<i>n</i> =33	<i>n</i> =7	

480

481 **Table 2.** List of rock forming minerals showing auxetic behaviour (Poisson's ratio < 0) in at least
 482 one direction. Also shown are those minerals with directions that have negative areal Poisson's
 483 ratio (Guo & Wheeler, 2006). The Reference column shows the source of the elasticity data for
 484 each mineral used in the calculation. The auxetic directions were found by calculating Poisson's
 485 ratio for every possible direction (α , β , θ in the Turley & Sines reference frame shown in Figure 1)
 486 using an angular increment of 1 degree in each direction.

487



488

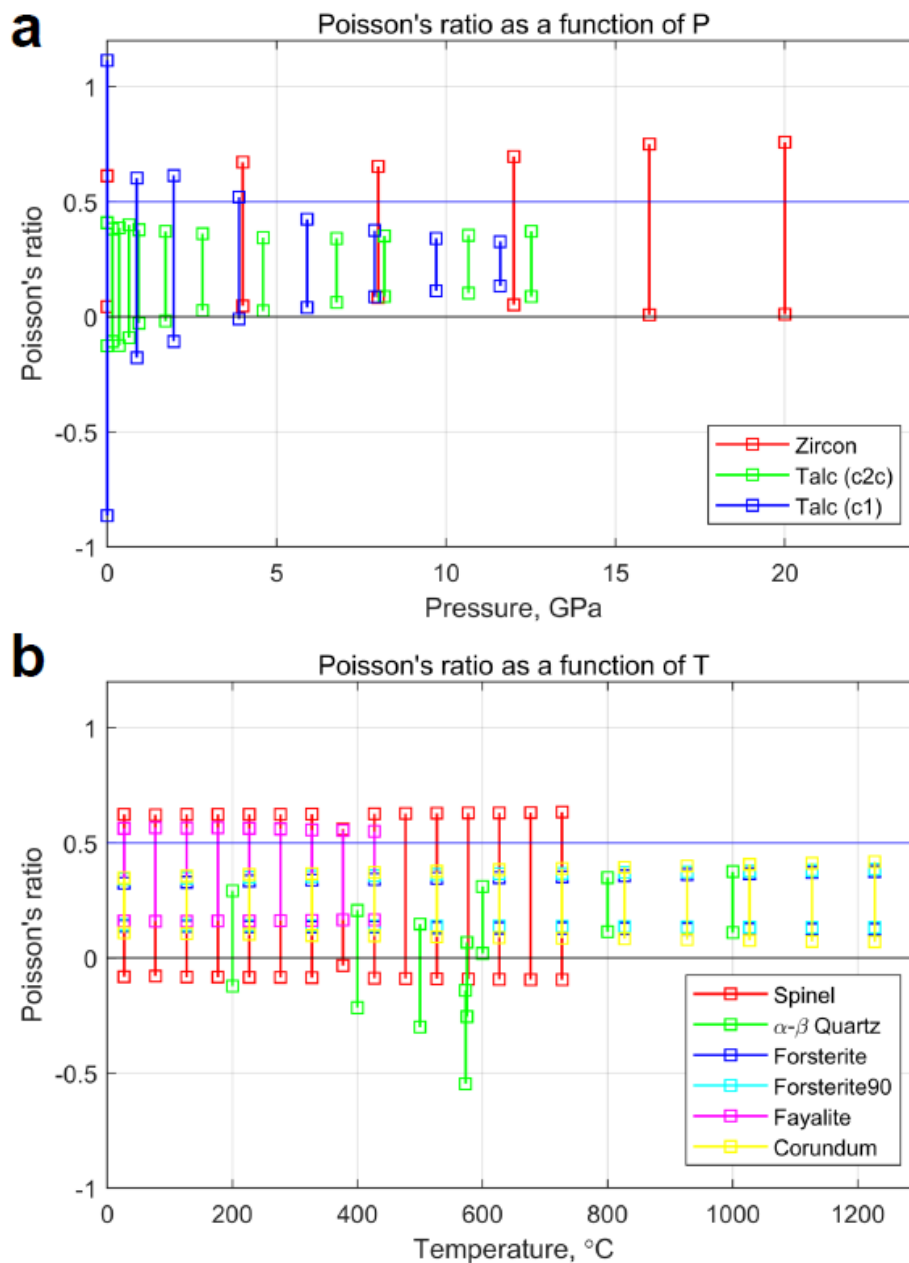
489 **Figure 14.** Examples of rock forming minerals showing auxetic and areally auxetic behaviour.
490 Stereograms are all lower hemisphere, equal area projections and only the directions with negative
491 Poisson's ratio (a, b, c, e, g) or negative areal Poisson's ratio (d, f, h) are shown coloured in (i.e.
492 other directions show positive values). Crystallographic axes in pink. **a)** Staurolite. **b)** Illite-
493 smectite. **c-d)** α -Quartz. **e-f)** α -Quartz at the temperature of the phase transformation to β -Quartz
494 (hexagonal). **g-h)** Talc (c1, triclinic).

495

496 The elastic properties of minerals are known to be temperature (T) and pressure (P) dependent.
497 However, systematic data to quantify the variation of anisotropic elasticity with T or P is relatively
498 scarce. We summarise some of the published data in Figure 15, shown as the calculated range in
499 Poisson's ratio (ν_{min} to ν_{max}). In terms of pressure dependence, the effect of increasing P is to
500 decrease the anisotropy in ν for talc to within the range normally expected for isotropic minerals.
501 The opposite effect is observed for zircon, with modest increases in ν_{max} with P . The temperature
502 dependence of elastic anisotropy in quartz is well known (Mainprice & Casey, 1990), with a



503 significant excursion into auxetic behaviour at the temperature of the α - β phase transition at 573°C
504 (846°K). The effect of increasing T on the anisotropy of ν for olivine, corundum and spinel is
505 almost non-existent.



506

507 **Figure 15.** Anisotropy of Poisson's ratio in rock-forming minerals as a function of P (top) and T
508 (bottom). Other than the well-known auxeticity of α - β quartz around the phase transition



509 (T=573°C), most minerals display Poisson’s ratios of between 0-0.5. Talc (c1, triclinic) is one
 510 exception, and the anisotropy of Poisson’s ratio decreases markedly with increasing P.

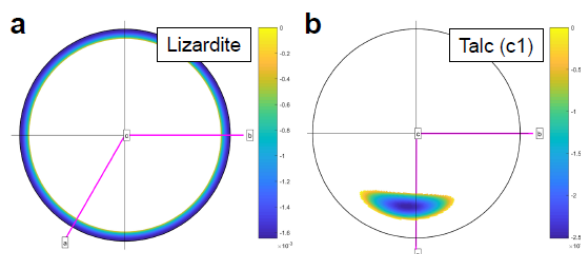
511 Linear compressibility (β) also displays significant anisotropy in rock forming minerals (Figure 17).
 512 A list of the rock forming minerals in our database that show negative linear compressibility (NLC)
 513 is shown in Table 3. These minerals have directions that expand in response to a compressive
 514 hydrostatic pressure (and vice versa: ‘stretch-densification’ of Baughman et al., 1998b). The
 515 specific directions of negative β are shown in the stereograms in Figure 16.

516

Mineral	Symmetry	Minimum $\beta < 0$, GPa ⁻¹	Reference
Lizardite	Hexagonal	-0.00165	Reynard et al., 2007
Talc (c1)	Triclinic	-0.00251	Mainprice et al., 2008

517

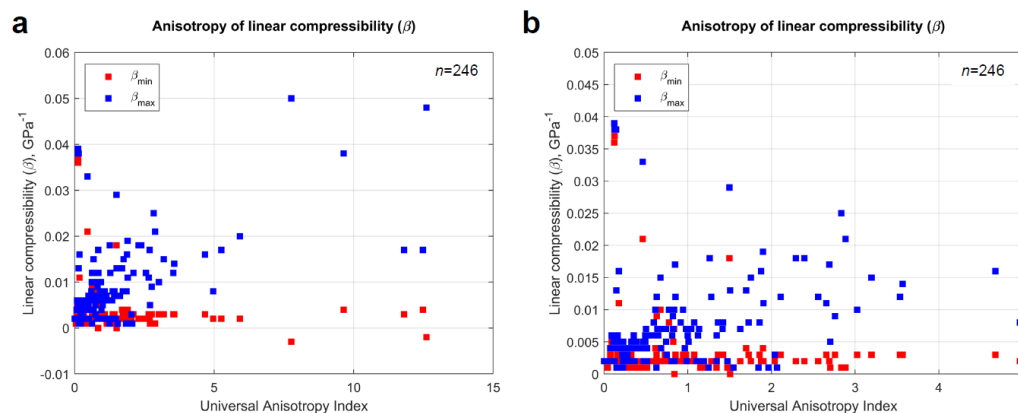
518 **Table 3.** List of rock forming minerals showing negative linear compressibility (NLC) in at least
 519 one direction.
 520



521

522 **Figure 16.** Rock forming minerals showing negative linear compressibility (NLC) in certain
 523 directions. Stereograms are all lower hemisphere, equal area projections and only the directions
 524 with NLC are shown coloured in (i.e. other directions show positive values). Crystallographic axes
 525 in pink. **a)** Lizardite. **b)** Talc (c1, triclinic).

526

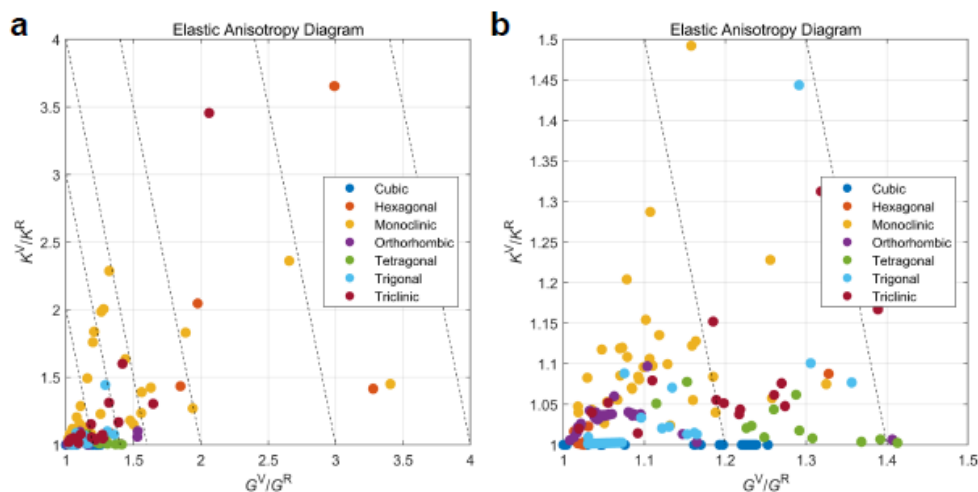


527

528 **Figure 17.** Anisotropy of linear compressibility in rock-forming minerals.



529 We can summarise the elastic anisotropy data for rock forming minerals using the Elastic
530 Anisotropy Diagram of Ranganathan & Ostoja-Starzewski (2008). In their review of Poisson's ratio
531 in materials, Greaves et al. (2011) used a plot of bulk modulus K versus shear modulus G , however
532 for the anisotropic rock forming minerals there is no single value of either of these properties. We
533 therefore take the ratios K^V/K^R and G^V/G^R and plot these instead (Figure 18). Unsurprisingly,
534 minerals with monoclinic, triclinic and hexagonal symmetries dominate the higher anisotropies,
535 while minerals with cubic, orthorhombic and tetragonal symmetries are generally less anisotropic.



536
537 **Figure 18.** a) Anisotropy of rock-forming minerals ($n=246$) using the Elastic Anisotropy Diagram
538 used in materials science, grouped by mineral symmetry class. b) Close-up of the data plotted in a),
539 in the range G^V/G^R 1 to 1.5 and K^V/K^R 1 to 1.5.

540

541 5. Results – Specific examples

542 *Twinning*

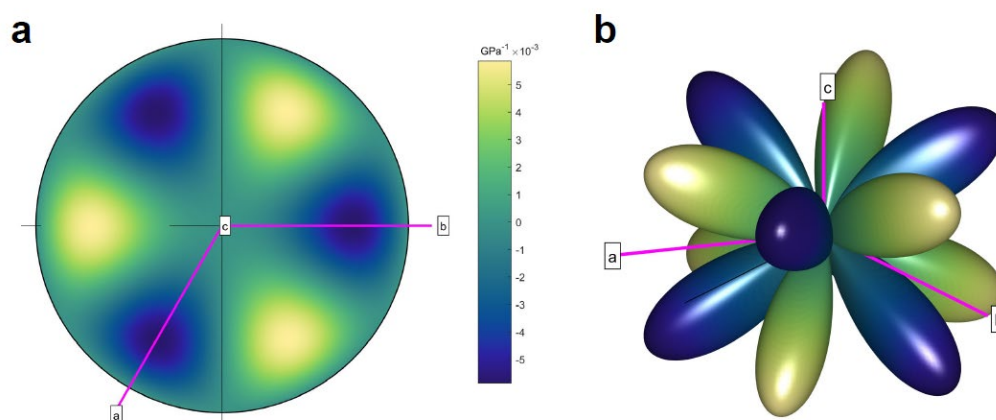
543 Deformation or mechanical twinning critically depends on the anisotropy of elastic properties
544 because minerals respond elastically to imposed stress (or strain) before exceeding the threshold for
545 twin nucleation and propagation (Christian and Mahajan, 1995, and references therein). Perhaps the
546 most widely accepted theory is that twin initiation occurs when an applied shear stress along the
547 twin shear plane (K_I) in the shear direction of twinning (η_1) reaches a critical value (critically
548 resolved shear stress, CRSS) for twin nucleation and propagation, analogous to Schmid's law for
549 dislocation slip (Thompson and Millard, 1952; Bell and Cahn, 1953; Christian and Mahajan, 1995).
550 However, experimental results can indicate that twinning dynamics can be more complex (e.g., Bell
551 and Cahn, 1957). Additional complexities, such as energy barriers for the nucleation of coeval
552 defects such as stacking faults, disconnections, and unstable transition states associated with
553 twinning, have also been considered for twinning in metals (e.g., Serra & Bacon, 1996; Kibey et al.,
554 2007; Pond et al., 2016). Development of a general theory of mechanical twinning applicable to
555 most minerals is still lacking. Nevertheless, shear modulus G in η_1 along K_I is highly relevant to
556 mechanical twinning.



557 Dauphiné twins in α -quartz are merohedral twins, meaning only some atoms exchange their
558 positions, resulting in a host-twin symmetry relationship that can be described simply by a 180°
559 rotation about the c-axis, and recognisable in EBSD maps via a 60° misorientation around the c-
560 axis. The formation of Dauphiné twins has been related to the difference in elastic strain energy
561 between twinned and un-twinned at constant stress (Thomas & Wooster, 1951; Tullis, 1970; De
562 Vore, 1970). This difference in elastic strain energy can be written as

$$563 \quad \Delta E = \frac{1}{2} (\sigma_1 - \sigma_3)^2 \Delta s_{11}' \quad (15)$$

564 where $(\sigma_1 - \sigma_3)$ is the applied differential stress, and $\Delta s_{11}' = s_{11}'^{\text{twinned}} - s_{11}'^{\text{un-twinned}}$. Note that s_{11}' is
565 the reciprocal of the Young's modulus for a given direction. Dauphiné twinning occurs more
566 readily in those directions for which the strain energy difference (ΔE) is larger, under a boundary
567 condition of constant axial stress (the inverse is also true: under a condition of constant strain, the
568 preferred directions of twinning are those that minimise ΔE (Paterson, 1973)). The variation of
569 $\Delta s_{11}'$ with direction in α -quartz is shown in Figure 19. The stereogram is the same pattern shown in
570 Thomas & Wooster (1951; their Figure 3a) and Tullis (1970; her Figure 2b). Also shown is a 3D
571 representation surface of $\Delta s_{11}'$, which emphasises the anisotropy of favoured directions for
572 Dauphiné twins in α -quartz. The significance of Dauphiné twinning in quartz has recently been
573 described for sandstones compacted during diagenesis (Mørk and Moen, 2007), deformed in fault
574 damage zones (Olierook et al., 2014), and deformed by meteorite impact (Wenk et al., 2011; Timms
575 et al., 2019; Cox et al., 2019), and granitoid protomylonites (Menegon et al., 2011). In all cases,
576 Dauphiné twins can be used to infer palaeostresses from deformed microstructures. In addition,
577 Menegon et al. (2011) make the point that Dauphiné twins, formed early in a deformation history,
578 may effectively store strain energy which is then consumed in later plastic deformation
579 mechanisms. De Vore (1970) plotted the directional variation of compliances for quartz, ortho- and
580 clino-pyroxene, hornblende and plagioclase and thereby extended the initial concept of Thomas &
581 Wooster (1951). To our knowledge, detailed analyses of mechanical twins in these phases has not
582 yet been related to the anisotropy of elastic compliance or the calculated variations in elastic strain
583 energy for specific applied loads.



584
585 **Figure 19.** Anisotropy of $\Delta s_{11}'$ for Dauphiné twinning in α -quartz. $\Delta s_{11}'$ is the difference in the
586 compliance s_{11}' between the twinned and un-twinned orientations for each direction. **a)** Stereogram
587 (lower hemisphere, equal area projection) and **b)** a 3D representation surface, both with the

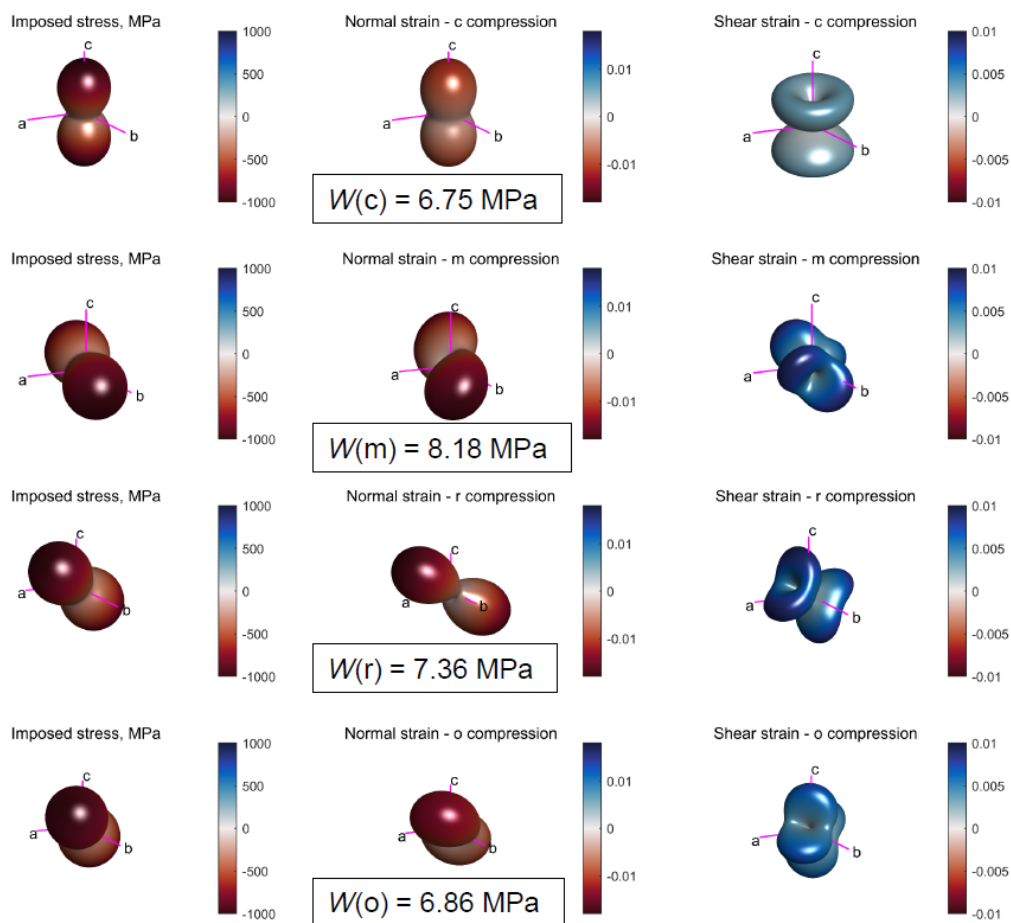


588 crystallographic reference axes marked. The directions represented by pale yellow/green colours
589 will be favoured for twinning, whereas the directions shown in blue will not.

590 The relationship between elastic anisotropy and deformation twinning has been investigated in
591 zircon (Timms et al., 2018). In zircon, deformation twins can form as a response to shock
592 conditions and are diagnostic of hypervelocity impact events (Timms et al., 2012; 2017; Erickson et
593 al. 2013). Shock twinning in zircon, which is tetragonal, can occur in up to four symmetrically
594 equivalent orientations, forming along $\{112\}$ composition planes (the of invariant shear, or K_1), and
595 with shear direction $\eta_1 = \langle 111 \rangle$, resulting in a host-twin $65^\circ / \{110\}$ misorientation relationship
596 (Timms et al., 2018). Twinning in this mode has been shown to correspond to the lowest values of
597 G ($G_{\min} = G_{\langle 111 \rangle} = \sim 98$ GPa) (Timms et al., 2018). Furthermore, the lowest values of ν are along
598 $\langle 111 \rangle$ in zircon, indicating that zircon is almost perfectly compressible in $\langle 111 \rangle$ ($\nu_{\min} = \nu_{\langle 111 \rangle} > 0$
599 and $\ll 0.1$) (Timms et al., 2018). These authors illustrate that elastic softness in shear (low G) and a
600 lack of lateral strain in the shear plane ($\nu \sim 0$) are favorable conditions for twinning in zircon
601 (Timms et al. 2018). However, further work is required to determine the critically-resolved shear
602 stress for twinning in zircon. Nevertheless, the ability to calculate and visualize anisotropic elastic
603 properties in specific crystallographic directions presented here will be very useful for detailed
604 investigations of mechanical twinning in other phases.

605 *Polymorphic phase transformations*

606 Coherent phase transformations (or transitions) may also be related to the anisotropy of elastic
607 properties, including the α - β transformation in quartz. Coe & Paterson (1969) describe experiments
608 on oriented cores from single crystals of quartz heated to temperatures above the transformation
609 temperature (573°C , at atmospheric pressure), and subjected to non-hydrostatic stress. They found
610 that the temperature of transition was raised by different amounts depending on the orientation of
611 the stress with respect to the crystal. Crystal cores stressed parallel to the c -axis showed the least
612 change, whereas those loaded in the m -direction (perpendicular to c) showed the greatest increase
613 (they also performed experiments on samples cored in the o and r' directions). The temperature of
614 phase transformation from α - (trigonal) to β - (hexagonal) quartz is therefore stress dependent. The
615 theoretical analysis of Coe & Paterson (1969, their Appendix C) ascribes this dependence to an
616 infinitesimal reversible transformation strain, based on the formalism of Eshelby (1957, 1959).
617 Noting that the transformation is also marked by a ‘dramatic increase in the development of small-
618 scale Dauphiné twins’, we have calculated the elastic strain energy per unit volume for each of the
619 four core orientations tested by Coe & Paterson, using their values of applied stress ($\sigma_1 = 1$ GPa, σ_2
620 $= \sigma_3 = 300$ MPa; all compressive) and the elastic constants of α -quartz at 500°C (Lakshtanov et al.,
621 2007). The results are shown in Figure 20, and clearly show an exact correlation with experimental
622 data: the sample loaded in the m direction has the highest strain energy, and that in the c direction
623 has the lowest. The overall sequence is $W(m) > W(r') > W(o) > W(c)$, which precisely mirrors that
624 of the variation in $\partial T / \partial \sigma$ listed for each direction in Coe & Paterson (1969, their Table 3).
625 Therefore, we speculate that the mechanism of phase transformation of α - to β - quartz may be
626 similar to that of Dauphiné twinning in α -quartz, and favoured for those directions that maximise
627 the elastic strain energy under a constant applied stress. We also note that similar processes may
628 occur in pyroxenes (Coe, 1970; Coe & Muller, 1973; Clement et al., 2018).



629 **Figure 20.** Variation in strain (normal and shear) and elastic strain energy for different applied
630 loads in α -quartz at 500 °C (Lakshtanov et al. 2007). The same compressive stress ($\sigma_1 = -1000$
631 MPa, $\sigma_2 = \sigma_3 = -300$ MPa) is applied along the *c* (row 1), *m* (row 2), *r* (row 3), and *o* (row 4)
632 directions in a single crystal. The Reynolds (2nd column) and HWY (3rd column) glyphs show the
633 normal and shear strains, respectively. The elastic strain energy per unit volume (W) is shown for
634 each configuration. Note that $W(m) > W(r) > W(o) > W(c)$.
635

636 Visualisation of elastic anisotropy has been used to gain new insights into the effects of intrinsic
637 elastic stiffness on the transformation from zircon to the high pressure ZrSiO₄ polymorph reidite
638 (Timms et al., 2018). The occurrence of lamellar reidite in shocked zircon from hypervelocity
639 impact structures has been observed to be spatially limited to low-U domains that have not
640 accumulated radiation damage of the lattice from the decay of U to Pb – a process known as
641 metamictization (Cavosie et al., 2015; Erickson et al., 2017). Using elastic constants measured for
642 variably metamict zircon (Özkan, 1976; Özkan and Jamieson, 1978), Timms et al. (2018) illustrated
643 that the process of metamictization significantly reduces maxima of E , G and ν in zircon resulting
644 in a compliant, isotropic structure. These authors argued that metamict domains in zircon grains are
645 not elastically stiff enough to support sufficiently high stresses and pressures to facilitate the
646 transformation to reidite, limiting reidite lamellae to highly crystalline non-metamict domains



647 during the same shock event. This finding illustrates the dependence of elastic properties on lattice
648 defects and a potential role of intrinsic elastic properties in phase transformations.

649 *Metamorphic reactions and equilibrium thermodynamics*

650 The role of elastic deformation in the thermodynamics of preferred orientations and reactions at the
651 scale of individual grains has long been controversial (Macdonald, 1960; Brace, 1960; Kamb, 1961
652 and discussion thereof; Paterson, 1973; Wheeler, 2017). Debate has centred on the role, if any, of
653 the elastic strain energy. W. Macdonald (1960) and Brace (1960) defined the Gibbs free energy of
654 non-hydrostatically stressed minerals in terms of the elastic strain energy, and thereby implicitly
655 defined equilibrium under these conditions. They went on to assert that preferred orientations
656 would develop by the (re-)orientation of a crystals in a given stress system such that their elastic
657 strain energies were maximised. Wheeler (2017), following Kamb (1961) and Paterson (1973),
658 asserts that there is no definable equilibrium in non-hydrostatically stressed systems. Therefore, it
659 is wrong to equate the Gibbs energy for stressed systems of polycrystals to the elastic strain energy.
660 Moreover, the contribution of the elastic strain energy to the chemical potentials along stressed
661 interfaces, through the Helmholtz free energy term, is second order and therefore negligible
662 (Wheeler, 2018).

663 *Brittle cracking, decrepitation and dehydration*

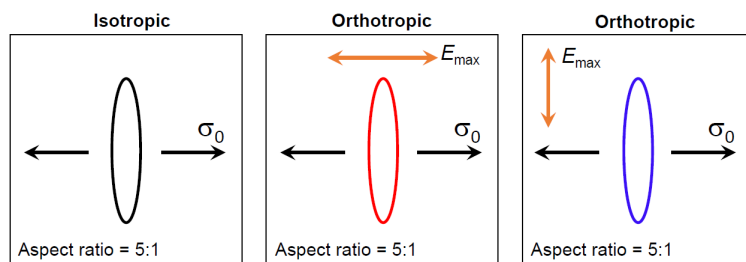
664 The magnitude of stresses around fluid-filled pores and cracks developed within single crystalline
665 grains under load can be important for a variety of natural processes. The decrepitation of fluid
666 inclusions occurs when the stresses around the pore exceed the local tensile strength, and the fluid
667 will then drain away. Previous analyses have been rooted in linear elastic fracture mechanics, under
668 an assumption of elastic isotropy. Similarly, in reacting systems the dehydration of hydrous phases
669 can lead to pore fluid overpressures which crack the reacting grain and produce dehydration
670 embrittlement (e.g. Raleigh & Paterson, 1965; Jung et al., 2004). Accurate predictions of the stress
671 levels sustainable by intracrystalline pores and cracks are therefore vital to understanding these
672 fundamental mechanisms. Jaeger & Cook (1969; and repeated by Pollard & Fletcher (2005))
673 asserted that the elastic anisotropy of rocks, measured as the ratio of Young's moduli E_{\max}/E_{\min} , is
674 rarely as high as 2, and therefore the effects of elastic anisotropy are minor to negligible. Davis et
675 al. (2017) used 3D boundary element models to show that Poisson's ratio and void (pore or crack)
676 shape can exert significant control on the local stresses at the void-matrix boundary as a precursor
677 to tensile or shear failure.

678 We have calculated the circumferential stresses around crack-like voids developed within single
679 elastically anisotropic grains of selected minerals (Figures 21-22). The model configuration follows
680 that of Jaeger & Cook (1969; derived from Green & Taylor, 1939), and is based on a thin 2D
681 orthotropic plate with a single crack of aspect ratio 5:1. The assumption of orthotropy reduces the
682 required elastic constants to five ($E_1, E_2, G, \nu_{21}, \nu_{12}$). We calculated the appropriate values of E, G
683 and ν from polar plots of anisotropy for the [010] crystallographic plane in each mineral using
684 AnisoVis (see Figure 4d, 5d, 5e-f). For an applied uniaxial tensile load (σ_0 in Figure 21) and a
685 plane strain assumption, the resulting anisotropy of circumferential stress ($\sigma_{\theta\theta}$) at the void-matrix
686 boundary is shown for four different minerals in Figure 22. Each polar plot shows the $\sigma_{\theta\theta}$
687 normalised by the applied load σ_0 in the [010] plane, and for two different configurations of the
688 anisotropy with respect to the load: σ_0 parallel to the direction of E_{\max} (red curves), and



689 perpendicular to the direction of E_{\max} (blue curves). For both of the hydrous sheet silicates talc (c1;
690 Mainprice et al., 2008) and lizardite (Reynard et al., 2007), the stresses display significant
691 anisotropy (Figure 22a and b), with amplifications of 6-7 times the stress predicted by assuming the
692 crystal is isotropic (black curves, calculated with VRH averages of E and ν). These stresses are
693 likely significant for the failure of cracks or narrow fluid-filled pores in dehydrating subducting
694 slabs (Healy et al., 2009; Ji et al., 2018). For the two feldspar examples, albite (Brown et al., 2016)
695 and sanidine (Waesermann et al., 2016), the amplification of circumferential stress is also
696 significant, at 4-5 times the isotropic prediction. Again, these stresses imply that fluid-filled pores
697 in phenocrysts of these phases may fail sooner than currently predicted under the assumption of
698 elastic isotropy. The restriction to 2D may appear limiting in these simple illustrative models, but
699 pending the development and analysis of fully 3D finite or boundary element models of stresses
700 around voids in elastically anisotropic media, they can provide useful insights into the relative
701 magnitude of local stresses and brittle failure. Moreover, we refute the suggestion from Jaeger &
702 Cook (1969) that as the anisotropy of Young's modulus in rocks is low, the anisotropy of stresses
703 around pores and cracks is therefore unimportant.

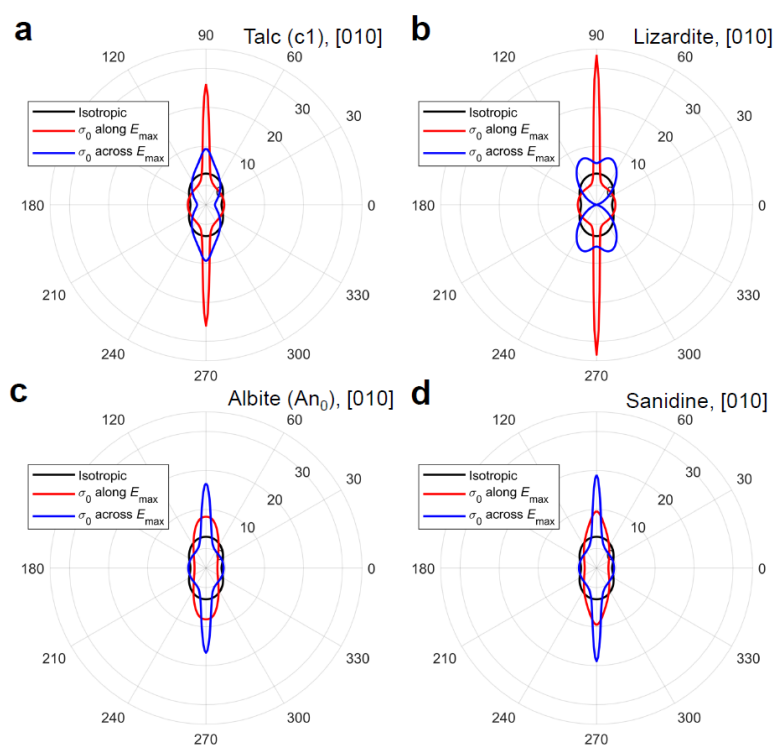
704



705

706 **Figure 21.** Schematic outline for models of narrow cracks in thin 2D orthotropic plates. The crack
707 is subjected to a uniaxial tensile stress, and plane strain is assumed. The colours of the crack
708 outlines correspond to the circumferential stress predictions in Figure 22.

709



710

711 **Figure 22.** Predictions of stresses around cracks in thin 2D orthotropic plates. Curves show the
712 directional variations in the circumferential stress ($\sigma_{\theta\theta}$) normalised by the applied uniaxial tensile
713 load (σ_0). **a)** Talc (c1, triclinic), [010] plane. **b)** Lizardite, [010] plane. **c)** Albite, [010]. **d)**
714 Sanidine, [010].

715

716 6. Summary

717 We reiterate a key point made by Marmier et al. (2010) in their analysis of chemical compounds:
718 it's only by visualising elastic anisotropies, preferably in 3D, that we can truly perceive them and
719 quantify their directions; this then allows us to relate these elastic properties to the underlying
720 crystal structure and explore the consequences for their behaviour. In developing AnisoVis and
721 using it to quantify the anisotropy of a specific mineral, we have presented multiple alternative
722 visualisations of the directional variation of commonly used elastic properties such as Young's
723 modulus (E), Poisson's ratio (ν), shear modulus (G) and linear compressibility (β). Used in
724 combination, these depictions serve to increase our understanding of the relationships between the
725 anisotropy of elastic properties and the underlying crystal symmetry and structure. We note that the
726 existence of directions with negative Poisson's ratios and negative linear compressibilities in certain
727 minerals (previously unreported). A potentially important consequence of these findings is that
728 there must also be specific directions along which these properties – Poisson's ratio or linear
729 compressibility – are 0. These directions will form surfaces in 3D which represents the boundary
730 between a) domains of positive and negative Poisson's ratio (both 'regular' and areal), along which
731 a uniaxially applied load will produce no lateral strain; and b) domains of positive and negative



732 linear compressibility, along which an applied hydrostatic load will produce no shortening or
733 stretching. These surfaces and directions in rock forming minerals may yet lead to new discoveries
734 in the physical behaviour of natural systems and novel applications in materials science or
735 engineering (e.g. Wu et al., 2015).

736 Considering the results from the database of 246 sets of elastic properties, we observe that:

- 737 • significant elastic anisotropy of rock forming minerals is much **more common** than previously
738 reported e.g. many minerals – 33 of the 86 we analysed – have auxetic directions, and some are
739 areally auxetic;
- 740 • the elastic anisotropy of rock forming minerals is **wider** than previously reported, with widely
741 assumed ‘natural limits’ frequently exceeded e.g. Poisson’s ratio for many minerals is either < 0
742 or > 0.5 .

743 For specific minerals, we also observe that

- 744 • elastic anisotropy has consequences for intracrystalline stresses under applied strain (and vice
745 versa); the difference between an assumption of isotropy and using the full elastic anisotropy is
746 often of the order of tens of MPa (even for small strains) – i.e. likely to be significant for the
747 deformation around voids such as pores and cracks, especially in dehydrating or decrepitating
748 systems;
- 749 • elastic anisotropy is important for mechanical (deformation) twinning, especially Dauphiné
750 twinning in quartz but probably in other minerals too;
- 751 • coherent phase transformations, such as the α - β transition in quartz, show a clear correlation
752 with the magnitude of elastic strain energy per unit volume and the stress dependence of the
753 transition temperature.

754 *Further work*

755 We are not currently limited by data; we need to process the elasticity data we have and use it to
756 improve our understanding of Earth processes. In theoretical terms, perhaps the biggest advance
757 would come from a solution to the Eshelby problem for an anisotropic inclusion in an anisotropic
758 host, for ellipsoids of general shape and orientation, for the points inside and outside the inclusion.
759 This problem is non-trivial but would be of direct relevance to the inclusion-host studies estimating
760 pressure histories, and for mechanical problems involving voids and cracks in anisotropic crystals,
761 including reacting systems. Numerical modelling studies of the deformation around voids and
762 cracks might usefully incorporate a wider range of values of E and ν . Visualisation of direction-
763 specific elastic properties will be useful for future investigations of the mechanics of twinning,
764 dislocations, and fractures in a wide range of minerals. Earthquake focal mechanisms are known to
765 depend on the elastic anisotropy of the source region (Vavrycuk, 2005), and better understanding of
766 the anisotropies in rock forming minerals is informing models of fabrics in subducting slabs (Li et
767 al., 2018) and interpretations of microseismicity from commercial hydraulic fracturing operations
768 (Jia et al., 2018). A practical assessment of the contribution of elastic strain energy to metamorphic
769 reactions might involve the systematic mapping of major element chemistry around specific
770 inclusions.

771 We believe that publicly available and easy-to-use software tools like AnisoVis may be useful in
772 teaching environments to guide understanding of the links between mineral properties (elastic,



773 acoustic, optical) and their underlying symmetry and lattice structure. Following Nye's original
774 text, other properties such as piezoelectric and thermal conductivities, could also be added and
775 visualised (Tommasi, 2001; Mainprice et al., 2015). Our AnisoVis MATLAB source code and
776 sample elasticity files have been made available in open repositories so that other developers and
777 researchers will optimise and extend the functionality, and that "given enough eyeballs, all bugs are
778 shallow" (Raymond, 1999).

779

780 **Code & Data Availability**

781 AnisoVis, including MATLAB source code, a basic user guide and data files for mineral elasticity
782 from published sources, is freely available on:

- 783 • GitHub (<https://github.com/DaveHealy-Aberdeen/AnisoVis>) and
- 784 • Mathworks FileExchange (<https://uk.mathworks.com/matlabcentral/fileexchange/73177-anisovis>).

785

786 **Author Contribution**

787 DH designed the software, and wrote the code to calculate the anisotropic elastic properties. NET
788 contributed most of the section on twinning. MAP contributed to the code, especially the
789 calculation of directional properties in Cartesian and crystallographic reference frames. All authors
790 contributed to the manuscript.
791

792

793 **Competing Interests**

794 The authors declare that they have no conflict of interest.

795

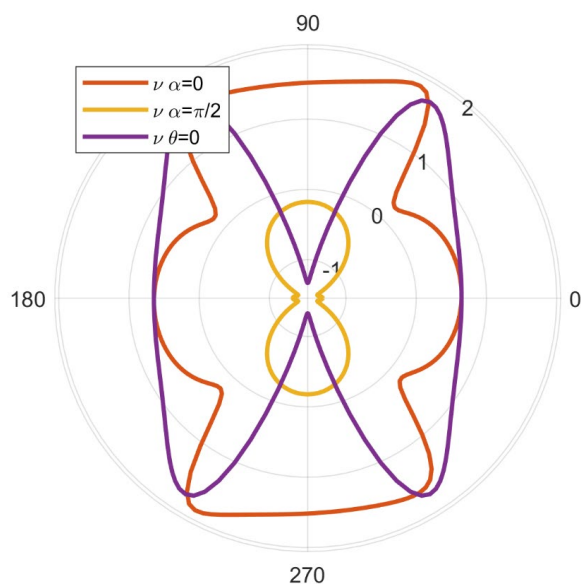
796 **Acknowledgements**

797 DH thanks John Wheeler (Liverpool) for discussion, and Ross Angel (Padua) for discussion and a
798 reprint. This paper is dedicated to the memory of John Frederick Nye (1923-2019) whose seminal
799 text book, first published in 1957 (Physical Properties of Crystals: Their Representation by Tensors
800 and Matrices; reprinted as Nye, 1985), has been a huge influence on the lead author. DH
801 acknowledges financial support from NERC (UK), grant NE/N003063/1.

802

803 **Appendix A – benchmarks to previously published anisotropic elastic properties**

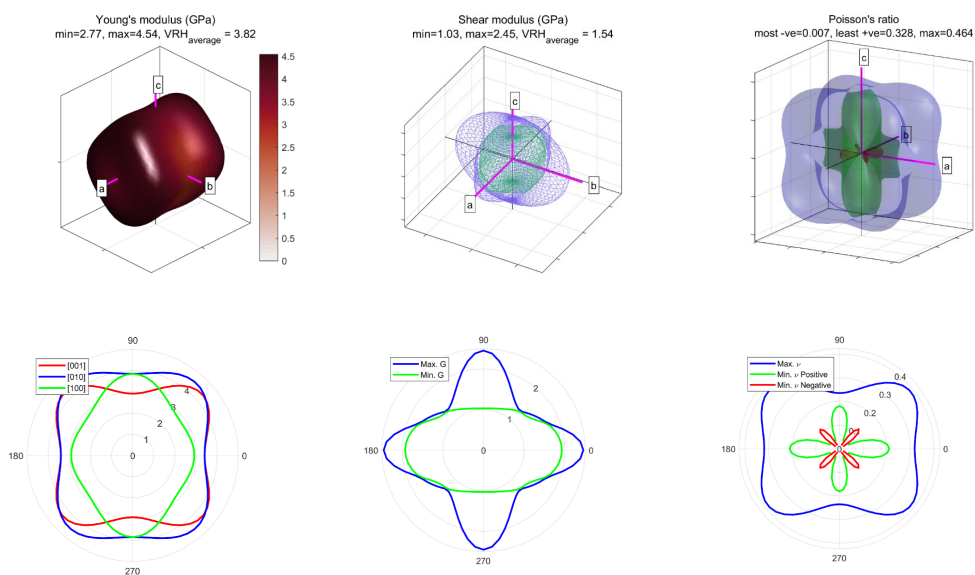
804 The outputs from AnisoVis, and the calculations underlying them, have been benchmarked against
805 previously published examples, chiefly from chemistry and materials science literature. Figures
806 produced by AnisoVis are shown below, with one example per symmetry group, formatted to
807 mimic the plots in the original publication.



808

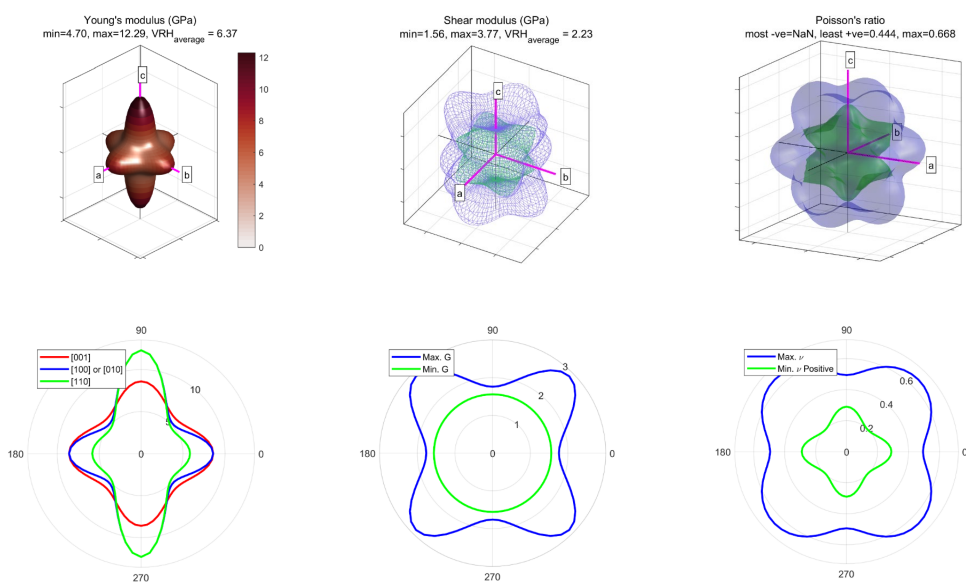
809 **Figure A1.** Benchmarks to Rovati (2004, their Figure 4) for monoclinic cesium dihydrogen
810 phosphate. Note the extreme auxeticity (negative Poisson's ratio) shown by this material.

811



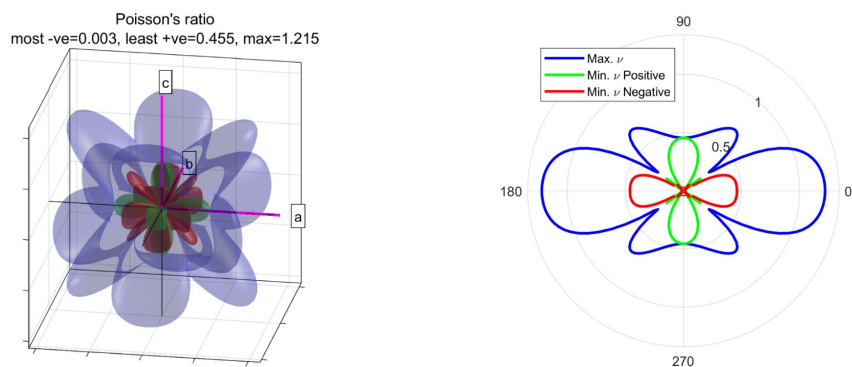
812 **Figure A2.** Benchmarks to Tan et al. (2015, their Figures 2, 3 and 4) for orthorhombic ZIF-4, a
813 zeolite. Plots shown for Young's modulus, shear modulus and Poisson's ratio.

814



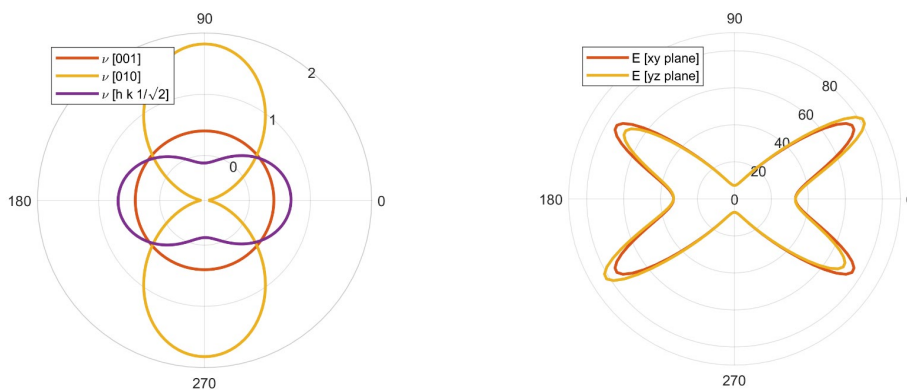
815 **Figure A3.** Benchmarks to Tan et al. (2015, their Figures 2, 3 and 4) for tetragonal ZIF-zni, a
816 zeolite. Plots shown for Young's modulus, shear modulus and Poisson's ratio.

817



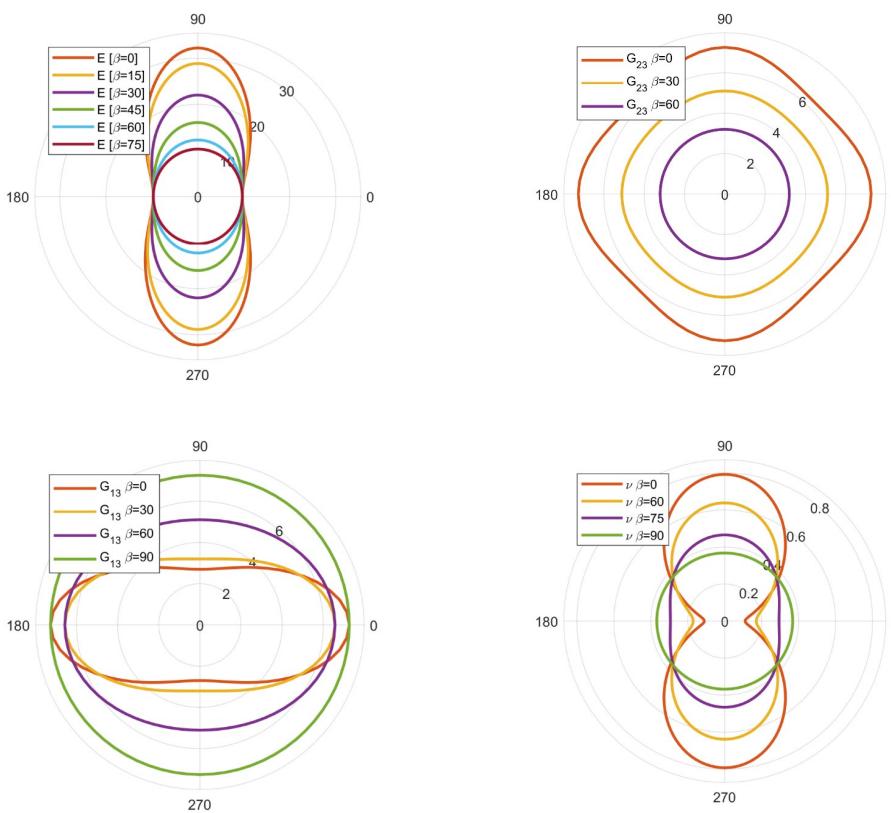
818 **Figure A4.** Benchmarks to Marmier et al. (2010, their Figure 5 and 6) for cubic cesium. Note the
819 auxetic nature of Poisson's ratio.

820

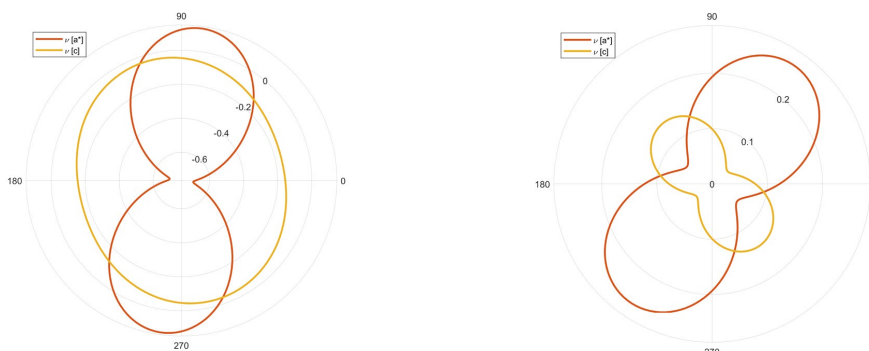


821 **Figure A5.** Benchmarks to Gunton & Saunders (1972, their Figures 3 and 6) for trigonal arsenic.

822



823 **Figure A6.** Benchmarks to Li (1976, their Figure 3) for hexagonal thallium.



824 **Figure A7.** Benchmarks to Mainprice et al. (2008, their Figure 5) for triclinic talc (c1) at 0.0 GPa
825 (left) and 3.9 GPa (right). The lower pressure example shows auxetic behaviour.

826

827 References

828 Aleksandrov, K.S., Ryzhova, T.V. & Belikov, B.P.: The elastic properties of pyroxenes. Soviet
829 Physics Crystallography, 8, pp.589-591, 1964.

830 Almqvist, B.S. & Mainprice, D.: Seismic properties and anisotropy of the continental crust:
831 predictions based on mineral texture and rock microstructure. Reviews of Geophysics, 55(2),
832 pp.367-433, 2017.

833 Anderson, O.L. & Isaak, D.G.: Elastic constants of mantle minerals at high temperature. Mineral
834 physics and crystallography: a handbook of physical constants, 2, pp.64-97, 1995.

835 Angel, R.J., Mazzucchelli, M.L., Alvaro, M., Nimis, P. & Nestola, F.: Geobarometry from host-
836 inclusion systems: the role of elastic relaxation. American Mineralogist, 99(10), pp.2146-2149,
837 2014.

838 Angel, R.J., Nimis, P., Mazzucchelli, M.L., Alvaro, M. & Nestola, F.: How large are departures
839 from lithostatic pressure? Constraints from host-inclusion elasticity. Journal of Metamorphic
840 Geology, 33(8), pp.801-813, 2015.

841 Aouni, N. & Wheeler, L.: Auxeticity of Calcite and Aragonite polymorphs of CaCO₃ and crystals
842 of similar structure. physica status solidi (b), 245(11), pp.2454-2462, 2008.

843 Babuska, V. & Cara, M.: Seismic anisotropy in the Earth (Vol. 10). Springer Science & Business
844 Media, 1991.

845 Bass, J.D.: Elastic properties of minerals, melts, and glasses. Handbook of Physical Constants,
846 pp.45-63, 1995.

847 Baughman, R.H., Shacklette, J.M., Zakhidov, A.A. & Stafström, S.: Negative Poisson's ratios as a
848 common feature of cubic metals. Nature, 392(6674), p.362, 1998a.



- 849 Baughman, R.H., Stafström, S., Cui, C. & Dantas, S.O.: Materials with negative compressibilities
850 in one or more dimensions. *Science*, 279(5356), pp.1522-1524, 1998b.
- 851 Bell, R. L., & Cahn, R. W.: The nucleation problem in deformation twinning. *Acta Metallurgica*,
852 1(6), 752-753, 1953.
- 853 Bell, R. L., & Cahn, R. W.: The dynamics of twinning and the interrelation of slip and twinning in
854 zinc crystals. *Proceedings of the Royal Society of London. Series A. Mathematical and Physical*
855 *Sciences*, 239(1219), 494-521, 1957.
- 856 Bezacier, L., Reynard, B., Bass, J.D., Sanchez-Valle, C. & Van de Moortèle, B.: Elasticity of
857 antigorite, seismic detection of serpentinites, and anisotropy in subduction zones. *Earth and*
858 *Planetary Science Letters*, 289(1-2), pp.198-208, 2010.
- 859 Birch, A.F. & Bancroft, D.: The elasticity of certain rocks and massive minerals. *American Journal*
860 *of Science*, 237(1), pp.2-6, 1938.
- 861 Brace, W.F.: Orientation of anisotropic minerals in a stress field: discussion. *Geological Society of*
862 *America Memoirs*, 79, pp.9-20, 1960.
- 863 Britton, T.B., Jiang, J., Guo, Y., Vilalta-Clemente, A., Wallis, D., Hansen, L.N., Winkelmann, A. &
864 Wilkinson, A.J.: Tutorial: Crystal orientations and EBSD—Or which way is up?. *Materials*
865 *Characterization*, 117, pp.113-126, 2016.
- 866 Brown, J.M., Angel, R.J. & Ross, N.L.: Elasticity of plagioclase feldspars. *Journal of Geophysical*
867 *Research: Solid Earth*, 121(2), pp.663-675, 2016.
- 868 Cavosie, A. J., Erickson, T. M., & Timms, N. E.: Nanoscale records of ancient shock deformation:
869 Reidite (ZrSiO₄) in sandstone at the Ordovician Rock Elm impact crater. *Geology*, 43(4), 315-318,
870 2015.
- 871 Chen, C.C., Lin, C.C., Liu, L.G., Sinogeikin, S.V. & Bass, J.D.: Elasticity of single-crystal calcite
872 and rhodochrosite by Brillouin spectroscopy. *American Mineralogist*, 86(11-12), pp.1525-1529,
873 2001.
- 874 Chopin, C.: Coesite and pure pyrope in high-grade blueschists of the Western Alps: a first record
875 and some consequences. *Contributions to Mineralogy and Petrology*, 86(2), pp.107-118, 1984.
- 876 Christian, J. W. & Mahajan, S.: Deformation twinning, *Progress in Materials Science*, 39, 1–57,
877 1995.
- 878 Christoffel, E.B.: Über die Fortpflanzung von Stößen durch elastische feste Körper. *Annali di*
879 *Matematica Pura ed Applicata* (1867-1897), 8(1), pp.193-243, 1877.
- 880 Clément, M., Padrón-Navarta, J.A., Tommasi, A. & Mainprice, D.: Non-hydrostatic stress field
881 orientation inferred from orthopyroxene (Pbc) to low-clinoenstatite (P 21/c) inversion in partially
882 dehydrated serpentinites. *American Mineralogist: Journal of Earth and Planetary Materials*, 103(6),
883 pp.993-1001, 2018.



- 884 Coe, R.S.: The thermodynamic effect of shear stress on the ortho-clino inversion in enstatite and
885 other coherent phase transitions characterized by a finite simple shear. *Contributions to mineralogy
886 and petrology*, 26(3), pp.247-264, 1970.
- 887 Coe, R.S. & Paterson, M.S.: The α - β inversion in quartz: a coherent phase transition under
888 nonhydrostatic stress. *Journal of Geophysical Research*, 74(20), pp.4921-4948, 1969.
- 889 Coe, R.S. & Muller, W.F.: Crystallographic orientation of clinoenstatite produced by deformation
890 of orthoenstatite. *Science*, 180(4081), pp.64-66, 1973.
- 891 Cox, M.A., Cavosie, A.J., Ferrière, L., Timms, N.E., Bland, P.A., Miljković, K., Erickson, T.M. &
892 Hess, B.: Shocked quartz in polymict impact breccia from the Upper Cretaceous Yallalie impact
893 structure in Western Australia. *Meteoritics & Planetary Science*, 54(3), pp.621-637, 2019.
- 894 Davis, T., Healy, D., Bubeck, A. & Walker, R.: Stress concentrations around voids in three
895 dimensions: The roots of failure. *Journal of Structural Geology*, 102, pp.193-207, 2017.
- 896 Deer, W., Howie, R. & Zussman, J.: *An introduction to the rock-forming minerals*. Essex. England:
897 Longman Scientific and Technology, 1992.
- 898 DeVore, G.W.: Elastic compliances of minerals related to crystallographic orientation and elastic
899 strain energy relations in twinned crystals. *Lithos*, 3(3), pp.193-208, 1970.
- 900 Erickson, T. M., Cavosie, A. J., Moser, D. E., Barker, I. R. & Radovan, H. A.: Correlating planar
901 microstructures in shocked zircon from the Vredefort Dome at multiple scales: Crystallographic
902 modeling, external and internal imaging, and EBSD structural analysis, *American Mineralogist*, 98,
903 53–65, 2013a.
- 904 Erickson, T. M., Pearce, M. A., Reddy, S. M., Timms, N. E., Cavosie, A. J., Bourdet, J. &
905 Nemchin, A. A.: Microstructural constraints on the mechanisms of the transformation to reidite in
906 naturally shocked zircon. *Contributions to Mineralogy and Petrology*, 172(1), 6, 2017.
- 907 Eshelby, J.D.: The determination of the elastic field of an ellipsoidal inclusion, and related
908 problems. *Proceedings of the Royal Society of London. Series A. Mathematical and Physical
909 Sciences*, 241(1226), pp.376-396, 1957.
- 910 Eshelby, J.D.: The elastic field outside an ellipsoidal inclusion. *Proceedings of the Royal Society of
911 London. Series A. Mathematical and Physical Sciences*, 252(1271), pp.561-569, 1959.
- 912 Gaillac, R., Pullumbi, P. & Coudert, F.X.: ELATE: an open-source online application for analysis
913 and visualization of elastic tensors. *Journal of Physics: Condensed Matter*, 28(27), p.275201, 2016.
- 914 Gercek, H.: Poisson's ratio values for rocks. *International Journal of Rock Mechanics and Mining
915 Sciences*, 44(1), pp.1-13, 2007.
- 916 Gillet, P., Ingrin, J. & Chopin, C.: Coesite in subducted continental crust: PT history deduced from
917 an elastic model. *Earth and Planetary Science Letters*, 70(2), pp.426-436, 1984.
- 918 Greaves, G.N., Greer, A.L., Lakes, R.S. & Rouxel, T.: Poisson's ratio and modern materials. *Nature
919 materials*, 10(11), p.823, 2011.



- 920 Green, A.E. & Taylor, G.I.: Stress systems in aeolotropic plates. I. Proceedings of the Royal Society
921 of London. Series A. Mathematical and Physical Sciences, 173(953), pp.162-172, 1939.
- 922 Gunton, D.J. & Saunders, G.A.: The Young's modulus and Poisson's ratio of arsenic, antimony and
923 bismuth. Journal of Materials Science, 7(9), pp.1061-1068, 1972.
- 924 Guo, C.Y. & Wheeler, L.: Extreme Poisson's ratios and related elastic crystal properties. Journal of
925 the Mechanics and Physics of Solids, 54(4), pp.690-707, 2006.
- 926 Hashash, Y.M., Yao, J.I.C. & Wotring, D.C.: Glyph and hyperstreamline representation of stress
927 and strain tensors and material constitutive response. International journal for numerical and
928 analytical methods in geomechanics, 27(7), pp.603-626, 2003.
- 929 Healy, D., Reddy, S.M., Timms, N.E., Gray, E.M. & Brovarone, A.V.: Trench-parallel fast axes of
930 seismic anisotropy due to fluid-filled cracks in subducting slabs. Earth and Planetary Science
931 Letters, 283(1-4), pp.75-86, 2009.
- 932 Hearmon, R.F.S.: The elastic constants of anisotropic materials. Reviews of Modern Physics, 18(3),
933 p.409, 1946.
- 934 Hearmon, R.F.S.: The third-and higher-order elastic constants. Numerical Data and Functional
935 Relationships in Science and Technology, Landolt-Bornstein, 11, 1979.
- 936 Hearmon, R.F.S.: The elastic constants of crystals and other anisotropic materials. Landolt-
937 Bornstein Tables, III/18, p.1154, 1984.
- 938 Hielscher, R. & Schaeben, H.: A novel pole figure inversion method: specification of the MTEX
939 algorithm. Journal of Applied Crystallography, 41(6), pp.1024-1037, 2008.
- 940 Hill, R.: The elastic behaviour of a crystalline aggregate. Proceedings of the Physical Society.
941 Section A, 65(5), p.349, 1952.
- 942 Jaeger, J.C. & Cook, N.G.: *Fundamentals of rock mechanics*. Methuen & Co. Ltd., London, 513,
943 1969.
- 944 Ji, S., Li, L., Motra, H.B., Wuttke, F., Sun, S., Michibayashi, K. & Salisbury, M.H.: Poisson's ratio
945 and auxetic properties of natural rocks. Journal of Geophysical Research: Solid Earth, 123(2),
946 pp.1161-1185, 2018.
- 947 Jia, S.Q., Eaton, D.W. & Wong, R.C.: Stress inversion of shear-tensile focal mechanisms with
948 application to hydraulic fracture monitoring. Geophysical Journal International, 215(1), pp.546-563,
949 2018.
- 950 Jung, H., Green Ii, H.W. & Dobrzhinetskaya, L.F.: Intermediate-depth earthquake faulting by
951 dehydration embrittlement with negative volume change. Nature, 428(6982), p.545, 2004.
- 952 Kamb, W.B.: The thermodynamic theory of nonhydrostatically stressed solids. Journal of
953 Geophysical Research, 66(1), pp.259-271, 1961.
- 954 Karki, B.B. & Chennamsetty, R.: A visualization system for mineral elasticity. Visual Geosciences,
955 9(1), pp.49-57, 2004.



- 956 Kern, H.: Elastic-wave velocity in crustal and mantle rocks at high pressure and temperature: the
957 role of the high-low quartz transition and of dehydration reactions. *Physics of the Earth and*
958 *Planetary Interiors*, 29(1), pp.12-23, 1982.
- 959 Kibey, S., Liu, J. B., Johnson, D. D. & Sehitoglu, H.: Predicting twinning stress in fcc metals:
960 Linking twin-energy pathways to twin nucleation, *Acta Mater.*, 55, 6843–6851, 2007.
- 961 Kratz, A., Auer, C. & Hotz, I.: *Tensor Invariants and Glyph Design. In Visualization and*
962 *Processing of Tensors and Higher Order Descriptors for Multi-Valued Data* (pp. 17-34). Springer,
963 Berlin, Heidelberg, 2014.
- 964 Lacazette, A.: Application of linear elastic fracture mechanics to the quantitative evaluation of
965 fluid-inclusion decrepitation. *Geology*, 18(8), pp.782-785, 1990.
- 966 Lakes, R.: Foam structures with a negative Poisson's ratio. *Science*, 235, pp.1038-1041, 1987.
- 967 Lakshtanov, D.L., Sinogeikin, S.V. & Bass, J.D.: High-temperature phase transitions and elasticity
968 of silica polymorphs. *Physics and Chemistry of Minerals*, 34(1), pp.11-22, 2007.
- 969 Lethbridge, Z.A., Walton, R.I., Marmier, A.S., Smith, C.W. & Evans, K.E.: Elastic anisotropy and
970 extreme Poisson's ratios in single crystals. *Acta Materialia*, 58(19), pp.6444-6451, 2010.
- 971 Li, Y.: The anisotropic behavior of Poisson's ratio, Young's modulus, and shear modulus in
972 hexagonal materials. *physica status solidi (a)*, 38(1), pp.171-175, 1976.
- 973 Li, J., Zheng, Y., Thomsen, L., Lapen, T.J. & Fang, X.: Deep earthquakes in subducting slabs
974 hosted in highly anisotropic rock fabric. *Nature Geoscience*, 11(9), p.696, 2018.
- 975 Lloyd, G.E. & Kendall, J.M.: Petrofabric-derived seismic properties of a mylonitic quartz simple
976 shear zone: implications for seismic reflection profiling. Geological Society, London, Special
977 Publications, 240(1), pp.75-94, 2005.
- 978 MacDonald, G.J.: Orientation of anisotropic minerals in a stress field. Geological Society of
979 America Memoirs, 79, pp.1-8, 1960.
- 980 Mainprice, D.: A FORTRAN program to calculate seismic anisotropy from the lattice preferred
981 orientation of minerals. *Computers & Geosciences*, 16(3), pp.385-393, 1990.
- 982 Mainprice, D. & Casey, M.: The calculated seismic properties of quartz mylonites with typical
983 fabrics: relationship to kinematics and temperature. *Geophysical Journal International*, 103(3),
984 pp.599-608, 1990.
- 985 Mainprice, D., Le Page, Y., Rodgers, J. & Jouanna, P.: Ab initio elastic properties of talc from 0 to
986 12 GPa: interpretation of seismic velocities at mantle pressures and prediction of auxetic behaviour
987 at low pressure. *Earth and Planetary Science Letters*, 274(3-4), pp.327-338, 2008.
- 988 Mainprice, D., Hielscher, R. & Schaeben, H.: Calculating anisotropic physical properties from
989 texture data using the MTEX open-source package. Geological Society, London, Special
990 Publications, 360(1), pp.175-192, 2011.



- 991 Mainprice, D., Bachmann, F., Hielscher, R., Schaeben, H. & Lloyd, G.E.: Calculating anisotropic
992 piezoelectric properties from texture data using the MTEX open source package. Geological
993 Society, London, Special Publications, 409(1), pp.223-249, 2015.
- 994 Mandell, W.: The determination of the elastic moduli of the piezo-electric crystal Rochelle salt by a
995 statical method. Proceedings of the Royal Society of London. Series A, Containing Papers of a
996 Mathematical and Physical Character, 116(775), pp.623-636, 1927.
- 997 Manghnani, M.H.: Elastic constants of single-crystal rutile under pressures to 7.5 kilobars. Journal
998 of Geophysical Research, 74(17), pp.4317-4328, 1969.
- 999 Mao, Z., Jiang, F. & Duffy, T.S.: Single-crystal elasticity of zoisite $\text{Ca}_2\text{Al}_3\text{Si}_3\text{O}_{12}(\text{OH})$ by
1000 Brillouin scattering. American Mineralogist, 92(4), pp.570-576, 2007.
- 1001 Marmier, A., Lethbridge, Z.A., Walton, R.I., Smith, C.W., Parker, S.C. & Evans, K.E.: ElAM: A
1002 computer program for the analysis and representation of anisotropic elastic properties. Computer
1003 Physics Communications, 181(12), pp.2102-2115, 2010.
- 1004 Mazzucchelli, M.L., Burnley, P., Angel, R.J., Morganti, S., Domeneghetti, M.C., Nestola, F. &
1005 Alvaro, M.: Elastic geothermobarometry: Corrections for the geometry of the host-inclusion
1006 system. Geology, 46(3), pp.231-234, 2018.
- 1007 Menegon, L., Piazzolo, S. & Pennacchioni, G.: The effect of Dauphiné twinning on plastic strain in
1008 quartz. Contributions to Mineralogy and Petrology, 161(4), pp.635-652, 2011.
- 1009 Militzer, B., Wenk, H.R., Stackhouse, S. & Stixrude, L.: First-principles calculation of the elastic
1010 moduli of sheet silicates and their application to shale anisotropy. American Mineralogist, 96(1),
1011 pp.125-137, 2011.
- 1012 Moore, J.G., Schorn, S.A. & Moore, J.: Methods of Classical Mechanics Applied to Turbulence
1013 Stresses in a Tip Leakage Vortex. Journal of turbomachinery, 118(4), pp.622-629, 1996.
- 1014 Mörk, M. B. E., & Moen, K.: Compaction microstructures in quartz grains and quartz cement in
1015 deeply buried reservoir sandstones using combined petrography and EBSD analysis. Journal of
1016 Structural Geology, 29(11), 1843-1854, 2007.
- 1017 Nye, J.F.: *Physical properties of crystals: their representation by tensors and matrices*. Oxford
1018 University Press, 1985.
- 1019 Ogi, H., Ohmori, T., Nakamura, N. & Hirao, M.: Elastic, anelastic, and piezoelectric coefficients of
1020 α -quartz determined by resonance ultrasound spectroscopy. Journal of Applied Physics, 100(5),
1021 p.053511, 2006.
- 1022 Olierook, H. K., Timms, N. E., & Hamilton, P. J.: Mechanisms for permeability modification in the
1023 damage zone of a normal fault, northern Perth Basin, Western Australia. Marine and Petroleum
1024 Geology, 50, 130-147, 2014.
- 1025 Özkan, H.: Effect of nuclear radiation on the elastic moduli of zircon. Journal of Applied Physics,
1026 47(11), 4772-4779, 1976.



- 1027 Özkan, H., & Jamieson, J. C.: Pressure dependence of the elastic constants of non-metamict zircon.
1028 *Physics and Chemistry of Minerals*, 2(3), 215-224, 1978.
- 1029 Pabst, W. & Gregorová, E.V.A.: Elastic properties of silica polymorphs—a review. *Ceramics-*
1030 *Silikaty*, 57(3), pp.167-184, 2013.
- 1031 Pasternak, E. & Dyskin, A.V.: Materials and structures with macroscopic negative Poisson's ratio.
1032 *International Journal of Engineering Science*, 52, pp.103-114, 2012.
- 1033 Paterson, M.S.: Nonhydrostatic thermodynamics and its geologic applications. *Reviews of*
1034 *Geophysics*, 11(2), pp.355-389, 1973.
- 1035 Pollard, D.D. & Fletcher, R.C.: *Fundamentals of Structural Geology*. Cambridge University Press,
1036 pp.512, 2005.
- 1037 Pond, R. C., Hirth, J. P., Serra, A., & Bacon, D. J.: Atomic displacements accompanying
1038 deformation twinning: shears and shuffles. *Materials Research Letters*, 4(4), 185-190, 2016.
- 1039 Prawoto, Y.: Seeing auxetic materials from the mechanics point of view: a structural review on the
1040 negative Poisson's ratio. *Computational Materials Science*, 58, pp.140-153, 2012.
- 1041 Raleigh, C.B. & Paterson, M.S.: Experimental deformation of serpentinite and its tectonic
1042 implications. *Journal of Geophysical Research*, 70(16), pp.3965-3985, 1965.
- 1043 Ranganathan, S.I. & Ostoja-Starzewski, M.: Universal elastic anisotropy index. *Physical Review*
1044 *Letters*, 101(5), p.055504, 2008.
- 1045 Raymond, E.: The cathedral and the bazaar. *Knowledge, Technology & Policy*, 12(3), pp.23-49,
1046 1999.
- 1047 Reynard, B., Hilaret, N., Balan, E. & Lazzeri, M.: Elasticity of serpentines and extensive
1048 serpentization in subduction zones. *Geophysical Research Letters*, 34(13), 2007.
- 1049 Rosenfeld, J.L.: Stress effects around quartz inclusions in almandine and the piezothermometry of
1050 coexisting aluminum silicates. *American Journal of Science*, 267(3), pp.317-351, 1969.
- 1051 Rosenfeld, J.L. & Chase, A.B.: Pressure and temperature of crystallization from elastic effects
1052 around solid inclusions in minerals?. *American Journal of Science*, 259(7), pp.519-541, 1961.
- 1053 Rovati, M.: Directions of auxeticity for monoclinic crystals. *Scripta materialia*, 51(11), pp.1087-
1054 1091, 2004.
- 1055 Rutter, E. H.: Pressure solution in nature, theory and experiment. *Journal of the Geological Society*,
1056 140(5), 725-740, 1983.
- 1057 Ryzhova, T. V.: Elastic properties of plagioclases, *Akad. SSSR Izv. Ser. Geofiz.*, 7, 1049–1051,
1058 1964.
- 1059 Serra, A., & Bacon, D. J.: A new model for {10 1 2} twin growth in hcp metals. *Philosophical*
1060 *Magazine A*, 73(2), 333-343, 1996.
1061



- 1062 Sinogeikin, S.V., Schilling, F.R. & Bass, J.D.: Single crystal elasticity of lawsonite. *American*
1063 *Mineralogist*, 85(11-12), pp.1834-1837, 2000.
- 1064 Tan, J.C., Civalleri, B., Erba, A. & Albanese, E.: Quantum mechanical predictions to elucidate the
1065 anisotropic elastic properties of zeolitic imidazolate frameworks: ZIF-4 vs. ZIF-zni.
1066 *CrystEngComm*, 17(2), pp.375-382, 2015.
- 1067 Tatham, D.J., Lloyd, G.E., Butler, R.W.H. & Casey, M.: Amphibole and lower crustal seismic
1068 properties. *Earth and Planetary Science Letters*, 267(1-2), pp.118-128, 2008.
- 1069 Thomas, L.A. & Wooster, W.A.: Piezoescence—the growth of Dauphiné twinning in quartz
1070 under stress. *Proceedings of the Royal Society of London. Series A. Mathematical and Physical*
1071 *Sciences*, 208(1092), pp.43-62, 1951.
- 1072 Thyng, K.M., Greene, C.A., Hetland, R.D., Zimmerle, H.M. & DiMarco, S.F.: True colors of
1073 oceanography: Guidelines for effective and accurate colormap selection. *Oceanography*, 29(3),
1074 pp.9-13, 2016.
- 1075 Timms, N.E., Healy, D., Reyes-Montes, J.M., Collins, D.S., Prior, D.J. & Young, R.P.: Effects of
1076 crystallographic anisotropy on fracture development and acoustic emission in quartz. *Journal of*
1077 *Geophysical Research: Solid Earth*, 115(B7), 2010.
- 1078 Timms, N. E., Reddy, S. M., Healy, D., Nemchin, A. A., Grange, M. L., Pidgeon, R. T., & Hart, R.:
1079 Resolution of impact-related microstructures in lunar zircon: A shock-deformation mechanism map.
1080 *Meteoritics & Planetary Science*, 47(1), 120-141, 2012.
- 1081 Timms, N.E., Erickson, T.M., Pearce, M.A., Cavosie, A.J., Schmieder, M., Tohver, E., Reddy,
1082 S.M., Zanetti, M.R., Nemchin, A.A. & Wittmann, A.: A pressure-temperature phase diagram for
1083 zircon at extreme conditions. *Earth-Science Reviews*, 165, pp.185-202, 2017.
- 1084 Timms, N.E., Healy, D., Erickson, T.M., Nemchin, A.A., Pearce, M.A. & Cavosie, A.J.: The role of
1085 elastic anisotropy in the development of deformation microstructures in zircon. In: Moser, D.,
1086 Corfu, F., Reddy, S., Darling, J., Tait, K. (Eds.), *AGU Monograph: Microstructural Geochronology;*
1087 *Lattice to Atom-Scale Records of Planetary Evolution*. AGU-Wiley, 183-202, 2018.
- 1088 Timms, N.E., Pearce, M.A., Erickson, T.M., Cavosie, A.J., Rae, A.S., Wheeler, J., Wittmann, A.,
1089 Ferrière, L., Poelchau, M.H., Tomioka, N. & Collins, G.S.: New shock microstructures in titanite
1090 (CaTiSiO₅) from the peak ring of the Chicxulub impact structure, Mexico. *Contributions to*
1091 *Mineralogy and Petrology*, 174(5), p.38, 2019.
- 1092 Thompson, N., & Millard, D. J.: Twin formation, in cadmium. *The London, Edinburgh, and Dublin*
1093 *Philosophical Magazine and Journal of Science*, 43(339), 422-440, 1952.
- 1094 Ting, T.C.T. & Chen, T.: Poisson's ratio for anisotropic elastic materials can have no bounds. *The*
1095 *quarterly journal of mechanics and applied mathematics*, 58(1), pp.73-82, 2005.
- 1096 Tommasi, A., Gibert, B., Seipold, U. & Mainprice, D.: Anisotropy of thermal diffusivity in the
1097 upper mantle. *Nature*, 411(6839), p.783, 2001.



- 1098 Tomé, C. N., & Lebensohn, R. A.: Manual for Code Visco-Plastic Self-Consistent (VPSC) (Version
1099 7c). Los Alamos National Laboratory, USA, 2009.
- 1100 Tullis, J.: Quartz: preferred orientation in rocks produced by Dauphiné twinning. *Science*,
1101 168(3937), pp.1342-1344, 1970.
- 1102 Turley, J. & Sines, G.: The anisotropy of Young's modulus, shear modulus and Poisson's ratio in
1103 cubic materials. *Journal of Physics D: Applied Physics*, 4(2), p.264, 1971.
- 1104 Van der Molen, I. & Van Roermund, H.L.M.: The pressure path of solid inclusions in minerals: the
1105 retention of coesite inclusions during uplift. *Lithos*, 19(3-4), pp.317-324, 1986.
- 1106 Vavryčuk, V.: Focal mechanisms in anisotropic media. *Geophysical Journal International*, 161(2),
1107 pp.334-346, 2005.
- 1108 Verma, R.K.: Elasticity of some high-density crystals. *Journal of Geophysical Research*, 65(2),
1109 pp.757-766, 1960.
- 1110 Waesermann, N., Brown, J.M., Angel, R.J., Ross, N., Zhao, J. & Kaminsky, W.: The elastic tensor
1111 of monoclinic alkali feldspars. *American Mineralogist*, 101(5), pp.1228-1231, 2016.
- 1112 Walker, A.M. & Wookey, J.: MSAT—A new toolkit for the analysis of elastic and seismic
1113 anisotropy. *Computers & Geosciences*, 49, pp.81-90, 2012.
- 1114 Weidner, D.J. & Carleton, H.R.: Elasticity of coesite. *Journal of Geophysical Research*, 82(8),
1115 pp.1334-1346, 1977.
- 1116 Wenk, H.R., Janssen, C., Kenkmann, T. & Dresen, G.: Mechanical twinning in quartz: shock
1117 experiments, impact, pseudotachylites and fault breccias. *Tectonophysics*, 510(1-2), pp.69-79,
1118 2011.
- 1119 Wheeler, J.: Importance of pressure solution and Coble creep in the deformation of polymineralic
1120 rocks. *Journal of Geophysical Research: Solid Earth*, 97(B4), 4579-4586, 1992.
- 1121 Wheeler, J.: The effects of stress on reactions in the Earth: Sometimes rather mean, usually normal,
1122 always important. *Journal of Metamorphic Geology*, 36(4), pp.439-461, 2018.
- 1123 Wu, Y., Yi, N., Huang, L., Zhang, T., Fang, S., Chang, H., Li, N., Oh, J., Lee, J.A., Kozlov, M. &
1124 Chipara, A.C.: Three-dimensionally bonded spongy graphene material with super compressive
1125 elasticity and near-zero Poisson's ratio. *Nature communications*, 6, p.6141, 2015.
- 1126 Yeganeh-Haeri, A., Weidner, D.J. & Parise, J.B.: Elasticity of α -cristobalite: a silicon dioxide with
1127 a negative Poisson's ratio. *Science*, 257(5070), pp.650-652, 1992.
- 1128 Zhang, Y.: Mechanical and phase equilibria in inclusion–host systems. *Earth and Planetary Science
1129 Letters*, 157(3-4), pp.209-222, 1998.
- 1130 Zhou, B. & Greenhalgh, S.: On the computation of elastic wave group velocities for a general
1131 anisotropic medium. *Journal of Geophysics and Engineering*, 1(3), pp.205-215, 2004.
- 1132